Journal of Electronic Imaging 14(4), 043005 (Oct–Dec 2005)

Linear color camera model for a skylight colorimeter with emphasis on the imaging pipeline noise performance

Panagiotis E. Haralabidis
Christodoulos Pilinis
University of the Aegean
Department of Environment
Mytilene, Greece 81100
E-mail: pharala@env.aegean.gr

Abstract. *We develop a digital camera model with the purpose of simulating the performance of a sky radiance colorimeter, based on a single-sensor camera equipped with a charge-coupled device imager. To provide a color image, the sensor is covered with a Bayer color filter array (CFA). The model input is the radiance, expressed in radiometric units. Demosaicking of the CFA is performed using three common interpolation methods. Color characterization is performed by calculating* 3×3 *matrices, based on either the maximum-ignorance assumption or computer-generated sky radiance training sets. For the model to be reliable, we incorporate multiple noise sources. We also parameterize many "critical" characteristics of the simulated imager, for example, temperature-related dark-current generation and pixel size. Error propagation analysis is performed, including an analysis for the demosaicking methods. Colorimetric performance results, expected measurement accuracy, and validation of the derived noise propagation equations are presented.* © 2005 SPIE and IS&T. [DOI: 10.1117/1.2137627]

1 Introduction

The presence of air-suspended particles (aerosols) is one of the main causes of observable discolorations and color contrast reduction of objects seen through a polluted atmosphere.[1,2] However, for the quantitative description of these tendencies, measurements of ambient atmospheric color are required.

In this paper, we investigate the possibility of using a color single-sensor camera to precisely record the color of the atmosphere. Sky color measurements can provide good estimates of the atmospheric clarity and contribute to the investigation of pollution episodes associated with low visibility. They can also provide useful information of the aerosol loading of the atmosphere.[1–5] Although recording sky color with a video or a still camera is not a new idea,[5,6] this is the first time research has been conducted on the characteristics of a camera used to record skylight. We are particularly interested in the investigation of the performance and characterization of a tristimulus colorimeter based on a single-sensor camera. This instrument is specifically intended to measure skylight color from various positions of the cloudless sky vault, during daytime including dawn and dusk hours.

Creating a digital camera model (DCM) that includes the simulation of noise sources is critical if we want to investigate the limitations of the measurement procedures. It is also important if we want to estimate the accuracy of color retrieval and know in advance the effect of noise on the camera output. Common scientific practice is the study of uncertainties for any measuring procedure.[7] In this paper, we are interested in the uncertainties of the measurements induced by the imaging pipeline itself, including the sensor thermal noise, and how these uncertainties influence accuracy. Furthermore, the sequence of the stages of the imaging pipeline progressively alters noise characteristics. As a result, once a noise source is inserted at any stage of the DCM pipeline, one should study its effects (error propagation) throughout the rest of the DCM.

The DCM developed by Vora *et al.*[8–11] has shown that DCMs can successfully simulate the operation of "real" cameras. However, only additive noise is included in the model and no analytical simulation of the various noise sources is attempted. Kolb *et al.*[12] presented a DCM that specifically addressed the issue of complex camera optics, but not the issue of noise. Wach and Dowski[13] presented a sensor-design-specific analytical method for describing the various sensor noise sources and emphasized on the readout noise. They assumed that all sensor pixels have the same response to light. This assumption is justified only for a particular type of sensor. Recently,[14,15] a model that incorporates extensive sensor and imaging pipeline parameterizations was presented. Although various noise sources are included in that DCM, the procedure is considered additive, and there is no discrimination between fixed pattern noise sources. All Poisson random processes are approximated by Gaussian distributions. This approximation performs well only for high illumination levels.

The most important stages of the proposed DCM are the optical system, the charge-coupled device (CCD) sensor simulation including the noise module, and the transformation of the sensor values to a device-independent color space. To form the red-green-blue (*RGB*) portions of a color image with a single-sensor camera, a color filter array (CFA) must be used. Since at each pixel of the sensor a single color is recorded, the remaining colors must be interpolated, using the color information from the neighboring pixels. This procedure is called demosaicking[16–18] and is another important stage of the DCM. In our noise module, we include a different flexible method for simulating

---

Paper 04189RR received Dec. 7, 2004; revised manuscript received Jun. 3, 2005; accepted for publication Jun. 27, 2005; published online Nov. 18, 2005.
1017-9909/2005/14(4)/043005/20/$22.00 © 2005 SPIE and IS&T.

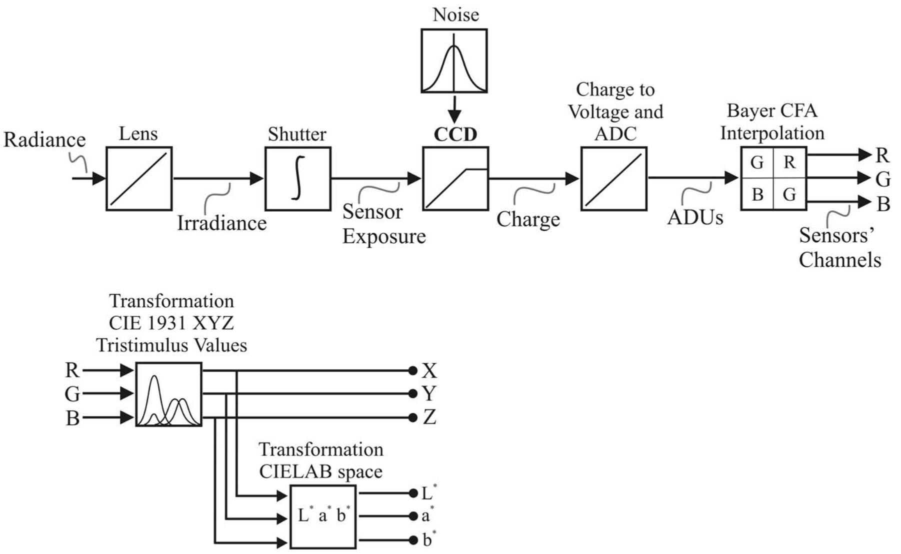

Fig. 1 Digital image pipeline used for modeling the color photographic camera using a single CCD image sensor.

additive and multiplicative noise sources. This method uses both Gaussian and Poisson number generators. As a result, it works for both high and low illumination levels. Furthermore, we distinguish between all the noise sources associated with the CCD operation, and therefore achieve broader parameterization. Model characterization is performed by using computer-generated, sky-specific spectral training sets. To calculate the appropriate 3×3 matrices that linearly transform sensor data to tristimulus values, we use three different methods. These methods are new application extensions of the methods described by Finlayson and Drew.[19] We prove that estimation of the transformation matrices using sky-related training sets can improve the accuracy of the skylight color measurements. We also performed error propagation analysis to investigate the noise performance of the DCM. We derived a set of equations that describes the noise propagation from its sources up to the output of the DCM, including the demosaicking procedure. We show that choosing the appropriate demosaicking procedure is important, since it alters the noise characteristics of the imaging pipeline.

Section 2 presents a short description of the DCM, while Sec. 3 presents the various stages of the DCM in detail. Specifically, in Sec. 3.1, we describe the optical system; in Sec. 3.2, we emphasize on the CCD modeling; and in Sec. 3.3, we focus on the noise module. Section 3.4 outlines the analog-to-digital conversion (ADC) module. Section 3.4 describes the formation of the Bayer CFA and the demosaicking strategies, while Sec. 3.5 discusses the matrix transformations. In Secs. 3.3, 3.5, and 3.6 we also present the error propagation equations. Finally, in Secs. 4.1 and 4.2, we test the colorimetric performance of the model and the accuracy of the derived noise propagation equations.

2 Model Description

Figure 1 shows a schematic of the single-sensor DCM imaging pipeline. The model simulates a linear color digital still camera (DSC) equipped with an *RGB* Bayer pattern,[20] which is a CFA widely used in various single-sensor devices. We concentrate our study on CCD sensors, because they exhibit better noise performance, compared to many complementary metal oxide semiconductor (CMOS) imagers, due to less on-chip circuitry.[21] CCDs are also considered as linear devices.[8,11,22] Although a small nonlinearity may exist, it can be corrected if a linearization step is added.

At the first stage of the model is the optical system. A single thin lens with an aperture stop is used. This simplification does not impose a problem, since sky is a target placed at an infinite distance from the observer, and clear sky has very low spatial content. Furthermore, a simplified optical system does not affect the noise performance of the sensor, the interpolation of a flat field image, or the color space transformations. However, the use of a lens system is necessary to estimate the correct exposure, given the lighting in the scene.[12] In this case the main purpose of the camera optics is the conversion of radiance L ($\mathrm{W\ cm^{-2}\ sr^{-1}}$) to irradiance E ($\mathrm{W\ cm^{-2}}$). Since this DCM will be used for sky color retrievals, as well as noise modeling, attention is paid to the units and their physical magnitudes. We preferred to use mixed SI (Système International) units, with units common to atmospheric physics and radiation transfer models, for compatibility and effortlessness. The shutter controls the exposure of the CCD surface.[23] In our model, the shutter is considered ideal, controlled only by the predetermined exposure time Δt, and it is not a function of position on the image plane. The shutter controls the amount of radiant energy Φ (in joules) that reaches the sensor surface.

Noise is injected in the model at the third stage of the DCM. A noise module was created to introduce the necessary data fluctuations. All noise and response characteristics are considered similar to those of the Kodak KAF-5101 CE image sensor.[24] A linear analog to digital step is necessary for the proper conversion of voltage to analog-to-digital units (ADUs). The useful digitization precision (number of bits) is limited by the noise performance of the sensor.[25]

During the fifth stage of the digital image pipeline, three demosaicking techniques are used to extract the three sensor (*RGB*) channels from the Bayer CFA. First, we used the bilinear interpolation (BI) algorithm,[26] which is a simple componentwise method.[27] The other two methods are called smooth hue transition interpolation[26,28] (SHTI) and effective color interpolation[29] (ECI). These algorithms are spectral model-based[16–18,29–31] as they utilize the essential spectral information. Since the model is intended for flat-field imaging there is no need to include edge sensing algorithms.[16–18,30–32] All methods incorporated in the DCM are nonadaptive.

The last stage of the DCM is the conversion of the sensor (*RGB*) values into the tristimulus XYZ, using CIE 1931 2-deg color matching functions[33] (CMFs). Since the model is used for sky targets, we have implemented least square regressions, incorporating sky specific information. We use 3×3 matrix transformations for calculating the transformation matrices.[34] Three different methods are used. These methods are based on the work of Finlayson and Drew[19] and are called accordingly, sky point preserving maximum ignorance least-squares regression (MaxIgnSPPLS), sky radiance least squares regression (SkyRadLS), and sky point preserving sky radiance least squares regression (SkyRadSPPLS). To evaluate color performance of the DCM we use CIE 1976 $L^*a^*b^*$ color space.[34,35] The DCM was created by using the Mathematica software.

Table 1 Image sensor specifications.[25]

KODAK KAF-5101CE Full-Frame Color CCD	
Number of active pixels	2654×1996
Pixel size	$6.8\ \mu\text{m}\times 6.8\ \mu\text{m}$
Saturation signal	40,000 electrons and 720 mV
Dynamic range	67 dB
Total sensor noise[a]	17 electrons
Total noise (sensor plus readout noise)[a]	23 electrons
Dark signal (normal-maximum)[a]	3–40 mV/s
Photoresponse nonuniformity (normal-maximum)[a,b]	8–15%
Charge transfer efficiency	0.999995
Horizontal clock frequency (data rate)	28 MHz

[a] Operational conditions are: temperature=333 K and integration time=33 ms.

[b] Peak-to-peak difference between the maximum and the minimum average signal levels of 146×146 blocks within the sensor.

3 Digital Image Pipeline

3.1 *Optical System and Radiometry*

For a single thin lens with transmittance T_{lens}, the monochromatic irradiance E_λ on the image plane, given the monochromatic radiance normal to the object plane $L(\lambda)$, is approximated by the image illumination equation[12,23]:

$$E_\lambda = \frac{\pi T_{\text{lens}} L(\lambda)}{4N^2(1+m/p)^2+1}\cos^4\theta. \tag{1a}$$

A small area S is projected from the object to the image plane, inclined at an angle θ to the optical axis. The $\cos^4$ factor describes the variation of irradiance across the image plane due to the lens, an effect known as natural vignetting,[23] and N is the relative aperture. Since the object plane is considered to be at infinity, the image magnification m is zero.[23] Since the lens is assumed to be symmetrical, the pupil magnification p is 1. Let θ_H and θ_V be the horizontal and vertical components of angle θ. In the case of a 2-D image plane, the image illumination equation becomes

$$E_\lambda = \frac{\pi T_{\text{lens}} L(\lambda)}{4N^2+1}\cos^4[\arctan(\tan^2\theta_H+\tan^2\theta_V)^{1/2}]. \tag{1b}$$

To create the image we need to introduce some sensor characteristics. Let f be the focal length. Let H_H and H_V (both in millimeters) be the horizontal and vertical dimensions of the CCD, respectively. All pixels form an array of $N_H\times N_V$ photosites, equally spaced on the CCD surface. The central photosite has indexing values (0,0), while the upper-right has $(+N_H/2,+N_V/2)$ and the lower-left has $(-N_H/2-1,-N_V/2-1)$. The two angles θ_H and θ_V are related to the pixel indexing numbers (n,l) by:

$$\theta_H = \arctan\left(\frac{H_H}{N_H f}n\right) \quad \left(n=-\frac{N_H}{2}-1,\ldots,0,\ldots,\frac{N_H}{2}\right), \tag{2a}$$

$$\theta_V = \arctan\left(\frac{H_V}{N_V f}l\right) \quad \left(l=-\frac{N_V}{2}-1,\ldots,0,\ldots,\frac{N_V}{2}\right). \tag{2b}$$

3.2 *Modeling the CCD Response to Radiance*

Quantum efficiency (QE) Q_λ^k at wavelength λ in nanometers is defined as the number of signal electrons (e^-) created per incident photon,[36] while k defines the recording channel, from a total of K sensor classes ($K=3$). A value of $k=1,2,3$ denotes the R, G, and B channels, respectively. According to Table 1, each photosite of the CCD is a square of area $A_p=6.8\times 6.8\ \mu\text{m}$. If we assume that the incident irradiance is constant across the photosite surface, the detector responsivity R_λ^k ($e^-\ \text{J}^{-1}\ \text{cm}^2$) at wavelength λ can be estimated by[36]

$$R_\lambda^k = \frac{\lambda 10^{-9} Q_\lambda^k A_p}{hc} \quad (k=1,2,3), \tag{3}$$

where c is the speed of light (m s^{-1}), h (J s) is the Planck constant, and 10^{-9} (m nm^{-1}) is a scaling factor.

To build a reliable DCM, we used many characteristics of the Kodak KAF-5101CE image sensor. Figure 2 displays the QE for the three channels.[24] To limit the QE of the red channel a near-IR (NIR) cutoff cover glass of 1 mm thickness is simulated. The glass transmittance G_λ is wavelength dependent (Fig. 2). The linear sensor response in that case becomes[11,34–37] (no optical blur):

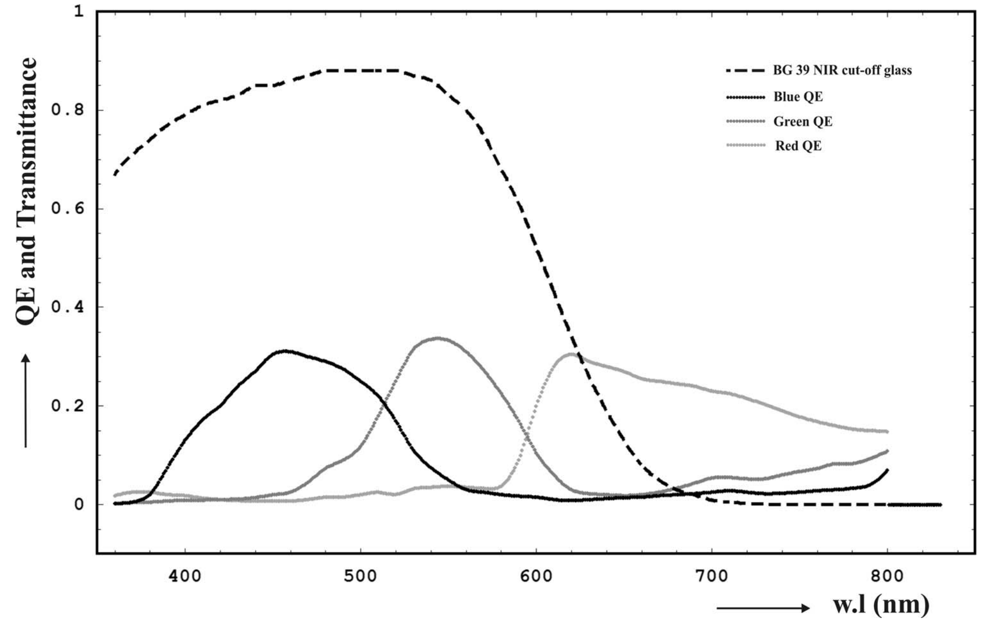

Fig. 2 Absolute QE curves for the Kodak KAF-5101 full-frame CCD color image sensor.[24] Transmittance of BG 39 glass is for thickness of 1 mm. Available at http://www.besoptics.com.

$$\rho_{n,l}^{k}=\int_{\lambda_{\min}}^{\lambda_{\max}} R_{\lambda}^{k} G_{\lambda} E_{\lambda}(n,l)\Delta t\,\mathrm{d}\lambda. \tag{4}$$

The shutter is open for a period Δt (in seconds) that determines the integration time, where the parameters $\lambda_{\min}$ and $\lambda_{\max}$ define the spectral band of our interest. All simulations are performed from $\lambda_{\min}=360$ nm to $\lambda_{\max}=830$ nm. The responses $\rho_{n,l}^{k}$ are measured in number of electrons. Note that the product of spectral irradiance E_{λ} (W cm^{-2} nm^{-1}) times the exposure time Δt times the pixel area A_p is equal to the spectral radiant energy Φ_{λ} (J nm^{-1}).

Regarding the imager geometry, we decided to use the popular 24- × 36-mm format with a variable number of pixels $N_H \times N_V$. The saturation signal of the imager ρ_{sat} is set at 40k electrons.[24]

To estimate the three *RGB* responses we must calculate Eq. (4). To do so we approximate the integral by a sum of terms. The spectral band $(\lambda_{\min},\lambda_{\max})$ is divided into evenly spaced sampling points $\lambda_j, \lambda_j+\Delta\lambda$ $(j=0,1,\ldots,M)$, where M is the total number of points. Radiance, QE, and glass transmittance become $L(\lambda_j)=L_j$, $Q_{\lambda_j}^{k}=Q_j^{k}$ and $G_{\lambda}=G_j$. Sampling interval is set[8] to $\Delta\lambda=1$ nm $(M=470)$. By merging Eqs. (1b), (3), and (4), we produce a set of equations that includes the optical system, the shutter and the CCD response $(k=1,2,3)$:

$$\rho_{n,l}^{k}=CC_{n,l}^{\text{opt}}\sum_{j=0}^{M}(\lambda_{\min}+j\Delta\lambda)Q_j^{k}G_jL_j, \tag{5a}$$

$$C_{n,l}^{\text{opt}}=\frac{\pi T_{\text{lens}}}{4N^2+1}\cos^4[\arctan(\tan^2\theta_H+\tan^2\theta_V)^{1/2}], \tag{5b}$$

$$C=\frac{A_p\Delta t\Delta\lambda}{hc}\times 10^{-9}. \tag{5c}$$

According to our experience, it is useful to exclude vignetting during the simulations, especially when we want to study the noise performance of the DCM. In that case, the term related to the camera optics $C_{n,l}^{\text{opt}}$ can be used leaving out the $\cos^4$ terms of Eq. (5b).

Three sensor responses are computed using Eqs. (5). This procedure is repeated for all the CCD photosites until three arrays $\mathbf{R}_S$, $\mathbf{G}_S$, and $\mathbf{B}_S$, of $N_H \times N_V$ elements each, are formed. As it is no longer necessary to use the n and l indexing, the usual i and j indices $(i=1,\ldots,N_V$ and $j=1,\ldots,N_H)$ are used from now on. All data produced at this stage of the DCM are forwarded to the noise module.

3.3 *Camera Noise Sources*

For the simulation of multiple noise sources, we used the Mathematica random number generators. Both Gaussian and Poisson distributions are used. We assumed that all noise sources that are not Poisson processes can be described by a Gaussian distribution. The various noise sources used in the DCM are[13,25,38,39]

1. Dark current shot noise (DCSN); a Poisson distribution is used.
2. Bulk dark current (BDC); in the model BDC, is injected through DCSN.
3. Dark current nonuniformity (DCNU); this noise results from the fact that each pixel generates a different amount of BDC. A Gaussian distribution is used to approximate the random differences between the CCD elements.
4. Signal shot noise (SSN); this is the fundamental limit of noise performance in light detection systems. A Poisson random generator is used.

5. Photoresponse nonuniformity (PRNU); this noise is caused by the fact that not all pixels demonstrate the same sensitivity to light. A Gaussian distribution is used.
6. Readout noise (RON); RON is independent of the measuring signal.[40] We assume that all other noise sources by the supporting circuitry are included under RON. A Gaussian distribution is used.

RON also includes output amplifier noise sources like white noise, and flicker or $1/f$ noise.[25] The $1/f$ noise has an inverse dependence on the sensor data rate. To simulate this noise source under RON we assume that the CCD operates under constant data rate as described in Table 1.

Another possible source of uncertainty, during the readout process, are the charge transfer efficiency[41] (CTE) and the related charge transfer inefficiency (CTI=1−CTE) of the sensor. Although CTI is not a noise source, it can degrade the image of the camera, especially when the sensor has a large number of pixels. We performed a number of simulations, taking into account the CTI effect. The color retrieval accuracy of the DCM was deteriorated. However, when we assumed that the CTE magnitude is constant, we were able to restore the recorded values. Simulation of the CTI was performed at this stage of the DCM, while cancellation of the CTI was performed after the ADC module. Since the effect of CTI can be corrected, we decided not to include it in this work. No other types of noise (e.g., reset noise) are considered, since methods of suppression exist.[32,40,41]

3.3.1 *Noise module*

This section describes the algorithm we created for the noise module. All noise parameters presented in this section are expressed in equivalent number of electrons.[39] We estimate the parameters of the noise module based on the specifications of KAF-5101CE sensor.[24]

Let I_{DC} (number of electrons pixel^{-1} s^{-1}) be the dark current generated on a photosite of area A_p (in centimeters squared) at operational temperature T in kelvins. The relation between BDC and temperature is given by the empirical formula[25]:

$$I_{\mathrm{DC}} = 2.5 \times 10^{15} A_P i_d T^{1.5} \exp[-E_g/(2kT)], \qquad (6)$$

where i_d (nA cm^{-2}) is the DC density defined[25] at 300 K, k (eV K^{-1}) is the Boltzmann constant, and E_g (in electronvolts) is the silicon bandgap. For the simulations presented here i_d was set equal to 0.068558 nA cm^{-2} and the CCD operational temperature was set[24] equal to 333 K. For a given exposure time Δt in seconds the total charge Q_{DC} (in number of electrons) caused by BDC is given by

$$Q_{\mathrm{DC}} = I_{\mathrm{DC}} \Delta t. \qquad (7)$$

We assume that the standard deviation σ is equal to the root mean square (rms) error or noise of the measured signal. Let Q_s (in number of electrons) be the light signal for a single pixel. Let σ_{DCNU} and σ_{PRNU} be the standard deviations of the DCNU and PRNU, respectively, modeled by the Gaussian random generator. Let σ_{RON} be the standard deviation of RON, modeled by the same generator. For DCSN and SSN the amount of noise introduced σ_{DCSN} and σ_{SSN} is equal to (Poisson distributions):

$$\sigma_{\mathrm{DCSN}} = \sqrt{Q_{\mathrm{DC}}}, \qquad (8a)$$

$$\sigma_{\mathrm{SSN}} = \sqrt{Q_S}. \qquad (8b)$$

It is convenient to describe the random generators as functions. The Gaussian generator $f_{\mathrm{norm}}(\sigma,\mu)$ is controlled by two parameters, the standard deviation σ and the mean value μ. The Poisson generator $f_{\mathrm{Poisson}}(\mu)$ is controlled only by the mean value. Each time the function is called, a random number is generated. To simulate the noise sources five arrays are created:

$$\mathbf{M}_{\mathrm{DCSN}} = \|m_{i,j}^{\mathrm{DCSN}}\| = \|f_{\mathrm{Poisson}}(Q_{\mathrm{DC}})\|, \qquad (9a)$$

$$\mathbf{M}_{\mathrm{DCNU}} = \|m_{i,j}^{\mathrm{DCSU}}\| = \|f_{\mathrm{norm}}(\sigma_{\mathrm{DCNU}},1)\|, \qquad (9b)$$

$$\mathbf{M}_{\mathrm{SSN}}^k = \|m_{i,j}^{\mathrm{SSN}}\| = \|f_{\mathrm{Poisson}}(\rho_{i,j}^k)\|, \qquad (9c)$$

$$\mathbf{M}_{\mathrm{PRNU}} = \|m_{i,j}^{\mathrm{PRNU}}\| = \|f_{\mathrm{norm}}(\sigma_{\mathrm{PRNU}},1)\|, \qquad (9d)$$

$$\mathbf{M}_{\mathrm{RON}} = \|m_{i,j}^{\mathrm{RON}}\| = \|f_{\mathrm{norm}}(\sigma_{\mathrm{RON}},0)\|. \qquad (9e)$$

Each of the preceding arrays contains the data fluctuations from a single noise source. Array $\mathbf{M}_{\mathrm{SSN}}^k$ contains the number of signal electrons calculated by Eq. (5) and the associated SSN. The mean values of the DCNU and PRNU random generators are set equal to 1 (μ=1). These arrays simulate the individual photosite capability to raise electrons due to BDC and incident light according to Eqs. (7) and (5). Note that a value of $\mu > 1$ indicates that more electrons would be collected than those expected by Eqs. (7) and (5). Similarly, a value of $\mu < 1$ indicates that less electrons would be collected than those expected by Eqs. (7) and (5). If we define operator * as the element wise multiplication of matrices, then matrix $\mathbf{M}^k = \|m_{i,j}^k\|$ is defined by

$$\mathbf{M}^k = \mathbf{M}_{\mathrm{DCSN}} * \mathbf{M}_{\mathrm{DCNU}} + \mathbf{M}_{\mathrm{SSN}}^k * \mathbf{M}_{\mathrm{PRNU}} + \mathbf{M}_{\mathrm{RON}}. \qquad (10)$$

The newly derived matrix $\mathbf{M}^k$ merges through Eq. (10) the CCD response to light and all the noise sources we wanted to model. The new data (with noise) produced are forwarded to the ADC module.

3.3.2 *Error propagation equation for the noise module*

For the noise module to be successful it must reproduce the typical photon transfer curve (PTC). In Appendix B, we derive the formulation that describes the error propagation of the noise module. We must keep in mind that all operators in Eq. (10) are element wise and no correlation exists between the noise sources. Implementing Eqs. (8)–(10) and by using basic error propagation equations[42] we can determine the standard deviation for the noise module (number of electrons):

$$f^k_{\mathrm{PTC}} = [Q_{\mathrm{DC}} + \bar{\rho}^k + (Q_{\mathrm{DC}}\sigma_{\mathrm{DCNU}})^2 + (\bar{\rho}^k\sigma_{\mathrm{PRNU}})^2 + (\sigma_{\mathrm{RON}})^2]^{1/2}, \tag{11}$$

where $\bar{\rho}^k$ is the mean electrons signal due to incident light. The last relationship defines the CCD noise floor and the signal levels that the model operates, being either shot noise or PRNU limited.

Running some preliminary simulations with no signal (i.e., $\bar{\rho}^k=0$), the noise floor of the CCD is set at $\sigma_{\mathrm{nf}} = 17.08$ electrons with $\sigma_{\mathrm{DCNU}}=0.2$. RON is estimated to be σ_{RON} equal to 15.7 electrons, giving an overall noise floor of 23.0 electrons.[24] Simulations are performed with $\sigma_{\mathrm{PRNU}}=0.008$ which results in peak to peak PRNU differences in the range of 8 to 15%. These differences were calculated performing simulations on all 2654×1996 imager pixels. The operating temperature is set to $T=333$ K. These results are consistent with the performance of the sensor, as described by the device specifications of Table 1.

3.4 *Linear Analog-to-Digital Conversion*

Let C_{vc} be the charge to voltage conversion factor. When multiplied with the signal, it provides the conversion from electrons to voltage (in millivolts). For the sensor modeled here,[24] $C_{\mathrm{vc}}=0.018$ mV/electron, and it is considered independent from the signal level and the color channel.

Let $F_{\mathrm{round}}(x)$ be a function that returns the closest integer of a real number x. Linear ADC expressed in ADUs is defined as a function $F_{\mathrm{ADC}}(\cdot)$:

$$F_{\mathrm{ADC}}(m^k_{i,j}) = F_{\mathrm{round}}(c_{\mathrm{bias}} + C_{\mathrm{vc}}a_{\mathrm{ADC}}m^k_{i,j}), \tag{12}$$

where $a_{\mathrm{ADC}}=3.268$ ADUs mV^{-1} being a constant that defines the slope of the mapping. Taking into account the CCD noise performance, a 12-bit ($n_{\mathrm{dig}}=12$) digitization is adequate. Since 12 bits introduce 4096 levels of signal (the ratio $\rho_{\mathrm{sat}}/\sigma_{\mathrm{nf}}$ is equal to 2342), and because DCM linearity is important, we choose to introduce a biasing parameter c_{bias} equal to 1753 ADUs. All parameters of Eq. (12) are the same for all sensor classes. The new matrices $\mathbf{M}^k_{\mathrm{ADU}} = \|m^k_{\mathrm{ADU},i,j}\|$ are of the form:

$$\mathbf{M}^k_{\mathrm{ADU}} = \|F_{\mathrm{ADC}}(m^k_{i,j})\|. \tag{13}$$

These matrices contain the digital code values of the camera. The noise characteristics are left unchanged during the ADC step. The signal and noise samples are simply converted from electrons into ADUs, multiplied by the $C_{\mathrm{vc}}a_{\mathrm{ADC}}$ factor.

3.5 *Bayer CFA Construction and Demosaicking*

So far we have constructed three distinct arrays of digital data, one for each sensor class. At this point, we can combine these arrays to simulate the Bayer CFA. We chose to incorporate a demosaicking stage in the DCM, because calculating the missing color components in the acquired CFA (sensor) image distorts the noise characteristics by introducing new demosaicked data.

Let $\mathbf{M}_{\mathrm{Bayer}}=\|m_{i,j}\|$ be the Bayer filter array of $N_V\times N_H$ elements. This array is formed by sampling $\mathbf{M}^R_{\mathrm{ADU}}$, $\mathbf{M}^G_{\mathrm{ADU}}$, and $\mathbf{M}^B_{\mathrm{ADU}}$, respectively, to construct the color format of the Bayer CFA.

Now $\mathbf{M}_{\mathrm{Bayer}}$ forms a gray-scale image due to the fact that only a single measurement is available at each spatial location.[17] The two missing components are calculated from the adjacent samples, using the BI, SHTI (Refs. 26 and 28), and the ECI (Ref. 29) demosaicking processes. SHTI is described as a constant hue-based interpolation.[26] Red and blue are the chrominance channels and green is the luminance channel, while hue is defined as the ratios R/G and B/G (Ref. 26). The hue modeling approach has been used in demosaicking,[17,30] single-sensor image zooming,[43] demosaicked image postprocessing,[44] and color image enhancement.[45] The ECI method can be viewed as SHTI variant, operating on R-G and B-G color differences, instead of the color ratios.[29] A short description of the algorithms is given in Appendix A. After the implementation of the interpolation methods, three color arrays $\mathbf{R}_{\mathrm{ADU}}$, $\mathbf{G}_{\mathrm{ADU}}$, and $\mathbf{B}_{\mathrm{ADU}}$, of $N_H\times N_V$ population are constructed. All elements of these three matrices are in units of ADUs, however, intermediate calculations are performed in float point arithmetic.

In the following paragraphs we present the derived noise propagation equations of the three demosaicking methods. Since these algorithms are framewise operations, the particular analysis is valid only when applied to a uniform portion of the image. Since the DCM is intended for flat-field imaging, the sensor image can be regarded as uniform.

3.5.1 *Noise performance of BI*

The standard deviation of the CFA data is altered by demosaicking. In Appendix C we estimate the noise outcome ($\sigma^{r,g,b}_{\mathrm{demos}}$) of BI:

$$\sigma^{r,g,b}_{\mathrm{demos}} = \sigma^{r,g,b}_{o}\left(\frac{n-1}{n'-1} + \frac{1}{m}\frac{n'-n-1}{n'-1}\right)^{1/2}, \tag{14}$$

where $\sigma^{r,g,b}_{o}$ is the initial error of the $\mathbf{M}_{\mathrm{Bayer}}$ RGB elements and m is the number of averaging neighbors during the interpolation. The exact population of a single color pixels is n, while the total population is $n'=N_H\times N_V$. According to Eq. (14), the implementation of BI results in statistically independent color channels. More approximate expressions of Eq. (14) are given in Appendix C.

3.5.2 *Noise performance of SHTI*

In order to estimate the error propagation of SHTI we must take into account parameters from other color channels, since this method uses multiple channels to extract a single color plane. Let n, v, and w be the exact populations of red, green, and blue elements of the CFA. In Appendix D the noise is estimated for the extracted chrominance planes ($\sigma^x_{\mathrm{demos}}$ becomes $\sigma^r_{\mathrm{demos}}$ for red and $\sigma^b_{\mathrm{demos}}$ for blue):

$$\sigma^x_{\mathrm{demos}} = \frac{1}{2}\left\{\frac{1}{(n'-1)}\left[(4n+2v+w-7)(\sigma^x_o)^2 + (6v+5w-11)\left(\frac{\bar{x}}{\bar{g}}\right)^2(\sigma^g_{\mathrm{demos}})^2\right]\right\}^{1/2}, \tag{15}$$

where $\bar{x}$ is the mean value of the chrominance plane interpolated, and $\bar{g}$ is the mean value of green channel. In bilinear interpolation the chrominance error generated by SHTI depends on the squared ratio $(\bar{x}/\bar{g})^2$ of the measurements

Table 2 Skyradiance samples generated by MODTRAN.

Number of Samples	MODTRAN Aerosol Type	Optical Path Zenith (deg)[a]	Optical Path Azimuth (deg)[b]	Greenwich Mean Time (GMT, h)
462	No aerosol	0–90, step 5 or 10	45–180, step 45	6–12, step 1 or 2
90	Rural[c] Vis=25 km	0–90, step 5 or 10	90 and 180	6–12, step 2
90	Rural Vis=5 km	0–90, step 5 or 10	90 and 180	6–12, step 2
90	Urban Vis=5 km	0–90, step 5 or 10	90 and 180	6–12, step 2
90	Tropospheric Vis=50 km	0–90, step 5 or 10	90 and 180	6–12, step 2
90	Marine Vis=23 km	0–90, step 5 or 10	90 and 180	6–12, step 2

[a] 90 is for horizontal optical path, 0 is for zenith view.

[b] Optical path azimuth (degrees east of north).

[c] Visibility (Vis) is defined as the meteorological range.

and the error $\sigma^{g}_{\text{demos}}$ of the demosaicked luminance plane. In Sec. 4 we discuss why this is a major problem.

During the various steps of the SHTI (as described in Appendix A), the participating color channels or hues are not always statistically independent. However, we derived Eq. (15) assuming independence. We did so because the derived equation still describes the main characteristics of the noise performance of the DCM while remaining simple and compact. According to Eq. (15) the implementation of SHTI affects the statistical dependence of the interpolated color channels. The elements of $\mathbf{R}_{\text{ADU}}$ and $\mathbf{B}_{\text{ADU}}$ are correlated with the elements of $\mathbf{G}_{\text{ADU}}$, while $\mathbf{R}_{\text{ADU}}$ and $\mathbf{B}_{\text{ADU}}$ are uncorrelated with each other. Approximations of Eq. (15) are provided in Appendix D.

3.5.3 *Noise performance of ECI*

This algorithm also exploits information from all color channels. The ECI method uses information from the red and blue channels to estimate the green pixels. Then ECI uses the demosaicked green channel to calculate the missing red and blue values. This forced us to take into account the presence of statistical correlations at certain ECI steps, in order to derive the noise performance. Let r_1 and r_2 be the correlation coefficients defined by Eq. (50). These coefficients describe the statistical dependence between R and B channels and the K_R and K_B domains. In Appendix E, the equation for the noise of the demosaicked green channel is derived:

$$\sigma^{g}_{\text{demos}} = \frac{1}{32}\{9(\sigma^{r}_{o})^2 + 20(\sigma^{g}_{o})^2 + 9(\sigma^{b}_{o})^2 + 4\sqrt{2}r_1\sigma^{r}_{o}[2(\sigma^{g}_{o})^2 + (\sigma^{r}_{o})^2]^{1/2} + 4\sqrt{2}r_2\sigma^{b}_{o}[2(\sigma^{g}_{o})^2 + (\sigma^{b}_{o})^2]^{1/2}\}^{1/2}. \quad (16)$$

We also estimated the noise output for the red or blue channel (the x and c notation is the same as SHTI) introducing the r'_1, r'_2, and r_3 correlation coefficients:

$$\sigma^{x}_{\text{demos}} = \frac{1}{16}\{9(\sigma^{x}_{o})^2 + 8(\sigma^{g}_{o})^2 + 5(\sigma^{g\rightarrow x}_{\text{add}})^2 + 4(\sigma^{\text{g}\rightarrow\text{c}}_{\text{add}})^2 - (8\sqrt{2}r'_1\sigma^{g}_{o} + 4r'_2\sigma^{\text{g}\rightarrow\text{c}}_{\text{add}})[(\sigma^{g\rightarrow x}_{\text{add}})^2 - 2r_3\sigma^{g\rightarrow x}_{\text{add}}\sigma^{x}_{o} + (\sigma^{x}_{o})^2]^{1/2} - 10r_3\sigma^{g\rightarrow x}_{\text{add}}\sigma^{x}_{o}\}^{1/2}. \quad (17)$$

Details for all the participating terms of Eqs. (16) and (17) including estimation of $\sigma^{g\rightarrow x}_{\text{add}}$, are given in Appendix E. Calculation of the magnitudes of the introduced r_1, r_2, r'_1, r'_2, and r_3 coefficients are presented in Sec. 4. Both equations do not include the populations of color pixels n, v, w, and n', as in the case of Eqs. (14) and (15). We derived Eqs. (16) and (17) assuming large CFA arrays to maintain a limited size for these equations. According to Eqs. (16) and (17), the application of ECI results in all color channels being statistically correlated. Approximate expressions of Eqs. (16) and (17) are provided in Appendix E.

3.6 *Color Space Transformations*

Since this DCM is intended for a specific application, sky specific radiance sets are needed for the estimation of the proper color-signal transformations. The use of atmospheric radiation transfer models is a standard method for realistic rendering of skylight and outdoor images.[46–48] To simulate skylight, for a variety of atmospheric conditions, we used[49] MODTRAN. A number of sky spectral radiance samples were obtained against various aerosol types (clear atmosphere, urban, rural, and marine), observer line-of-site zenith and azimuth angles, as well as day hours (sun geometry). The set consists of 912 radiance sets (at 1-nm intervals), all calculated for the same midlatitude geographic coordinates and for the 1976 U.S. standard atmosphere. Details of the computer generated radiance samples are given in Table 2. The CIE xy chromaticities of the simulated skylight (Fig. 3), exhibit similar scatter as real experimental data obtained by others.[49]

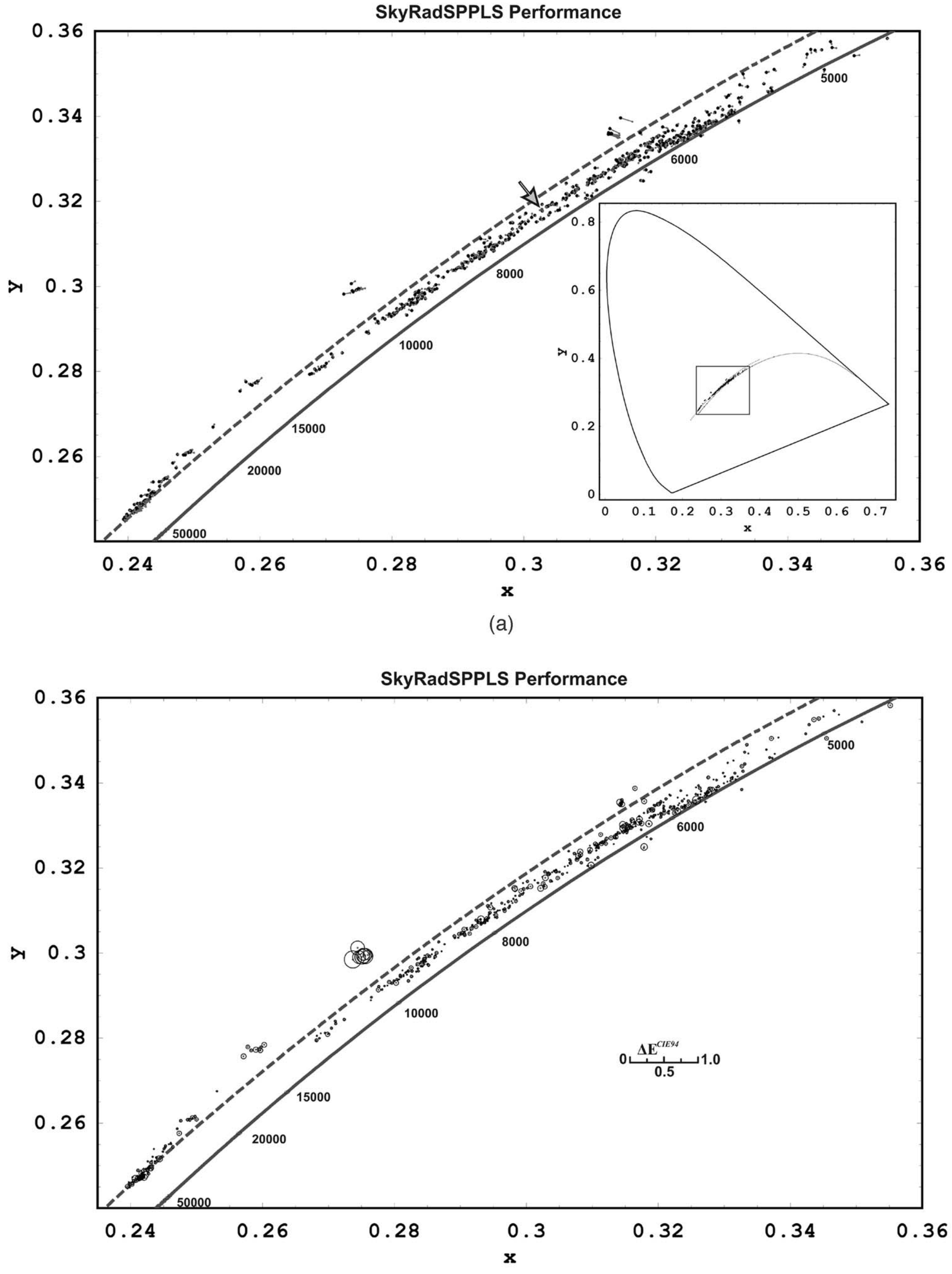

Fig. 3 (a) CIE 1931 *x* and *y* chromaticities of 912 simulated skylight spectra and SkyRadSPPLS colorimetric performance. Planckian locus (Solid line) overlaid with the Granada clear skylight locus[50] (dashed line). Gray lines present the errors of the transformation matrix (most of them are too small to distinguish). The arrow points the color of the sky used to constrain regressions. The inset shows the entire CIE 1931 diagram. (b) CIE 1931 *x* and *y* chromaticities and $\Delta E^{\mathrm{CIE94}}$ color difference cycles. The diameter of each circle is equal to the CIE-94 color deference of the color represented by a point at the center of the cycle. The circles and the scale are enlarged to be visible.

The color characterization of the DCM is performed using three different least square methods. The first method is a simple SkyRadLS that uses only the information from a limited training dataset as described in Refs. 19 and 34. The next two methods are new applications of the constrained least square regressions.[19] For the MaxIgnSPPLS, we estimate the appropriate transformation matrix by utilizing knowledge of the sensor responses (maximum ignorance), plus the constraint of preserving the tristimulus values of a single skylight radiance sample. The last method is the SkyRadSPPLS. We use the same set, as in SkyRadLS with the same constraint of the MaxIgnSPPLS.

Since the preceding training set is a subset of the initial 912 radiances, we had to determine the number of the initial skylight samples to be used. Principal value decomposition of skylight spectral power distributions (SPDs) for various atmospheric conditions and observer-sun geometries reveal strong correlations between samples.[50] As a result, the use of a small number of training samples is adequate for completely describing the proper nonmean subtracted covariance matrix that determines the linear regression.[19] In our case, we found that 20 spectral radiance samples are adequate. Extensive calculations with different or more populated training sets, gave little or no improvement of the colorimetric characterization. For the constrained skylight point we used one that represents the average values of aerosol loading and sun-observer geometry.

Let $\boldsymbol{\rho}^T$ be the imager 1×3 row vector output in ADUs. Let X, Y, and Z be the CIE 1931 tristimulus values calculated from the CIE $\bar{x}$, $\bar{y}$, and $\bar{z}$ CMFs, respectively.[35]

Row vector $\mathbf{x}^T$ is defined as $\mathbf{x}^T=[X,Y,Z]$. By using regression we calculated the 3×3 matrix $\mathbf{M}$ that linearly relates the sensor responses with the tristimulus values calculated for the same radiance. The colorimetric performance of the fit for a particular color is judged upon:

$$\mathbf{x}^T \simeq \boldsymbol{\rho}^T \mathbf{M}. \tag{18}$$

3.6.1 *Noise propagation during color space transformations*

For the noise analysis of the DCM to be complete, the error output of such transformations for a given noise level must be estimated. Let $\boldsymbol{\Delta\rho}=[\sigma^r_{\text{demos}},\sigma^g_{\text{demos}},\sigma^b_{\text{demos}}]$ be the 3×1 column vector of standard deviations for the sensor responses. The XYZ transformation results in tristimulus data $\mathbf{x}$ that suffer from the inherent noise of the initial $\boldsymbol{\rho}$ data. Let $\boldsymbol{\Sigma}_{\boldsymbol{\rho}}$ be the covariance matrix of all $\boldsymbol{\rho}^T$ signals. The corresponding covariance matrix of $\mathbf{x}^T$ from multivariable statistics[51] is $\boldsymbol{\Sigma}_{\mathbf{x}}=\mathbf{M}^T\boldsymbol{\Sigma}_{\boldsymbol{\rho}}\mathbf{M}$. When the signals $\mathbf{x}^T$ are regarded as statistically independent, the matrix $\boldsymbol{\Sigma}_{\mathbf{x}}$ becomes diagonal. The 3×1 error vector $\boldsymbol{\Delta}\mathbf{x}$ that contains the standard deviations of $\mathbf{x}^T$ can be estimated from $\boldsymbol{\Delta\rho}$:

$$(\boldsymbol{\Delta}\mathbf{x}^{\mathrm{T}})^2=(\boldsymbol{\Delta\rho}^{\mathrm{T}})^2 \cdot \mathbf{M}^2. \tag{19}$$

The square power notation of the above equation is an element-wise operation.

When the signals are statistically correlated, the $\boldsymbol{\Sigma}_{\boldsymbol{\rho}}$ matrix must be defined. We create $\boldsymbol{\Sigma}_{\boldsymbol{\rho}}$ using three correlation coefficients r_{rg}, r_{rb}, and r_{gb} according to Eq. (2). Each coefficient describes the correlation between red-green, red-blue, and green-blue demosaicked channels, respectively:

$$\boldsymbol{\Sigma}_{\boldsymbol{\rho}}=\begin{bmatrix} (\sigma^r_{\text{demos}})^2 & r_{rg}\sigma^r_{\text{demos}}\sigma^g_{\text{demos}} & r_{rb}\sigma^r_{\text{demos}}\sigma^b_{\text{demos}} \\ r_{rg}\sigma^r_{\text{demos}}\sigma^g_{\text{demos}} & (\sigma^g_{\text{demos}})^2 & r_{gb}\sigma^g_{\text{demos}}\sigma^b_{\text{demos}} \\ r_{rb}\sigma^r_{\text{demos}}\sigma^b_{\text{demos}} & r_{gb}\sigma^g_{\text{demos}}\sigma^b_{\text{demos}} & (\sigma^b_{\text{demos}})^2 \end{bmatrix}. \tag{20}$$

4 Simulation Results

In the next few paragraphs we present the results from a number of simulated measurements. In particular, we test the colorimetric performance of the DCM and compare the derived noise propagation equations against the operation of the DCM. All simulations were conducted with the parameters of the model set, as described in the previous sections.

4.1 *DCM Color Output*

In all the simulations we performed to assess the colorimetric performance of the DCM, the noise module is activated and the vignetting effect is excluded. To calculate the correct DCM response, a simulated dark frame is subtracted from the illuminated flat field image. CIELAB color space coordinates are estimated from the chromaticities calculated by CIE 1931 CMFs. These results are compared against the output of the DCM. The comparison is performed using the MaxIgnSPPLS, SkyRadLS, and SkyRadSPPLS transformations and the BI, SHTI, and ECI algorithms, by calculating the Euclidean distance[35] ΔE^*_{ab}. These results are converted into just noticeable differences (JNDs) by dividing by 2.3. Since CIELAB color space is only approximately uniform, we also calculated color differences using the CIE-94 color difference formulae.[34] We tested the DCM for all 912 samples and for 15×20 CCD pixels. All simulations are conducted at 3/4 of the saturation signal independent of the color channel. The wavelength interval $(\Delta\lambda)$ is 1 nm and the exposure time (Δt) is 0.033 s.

Results for the described simulations are illustrated in Fig. 3(a) and 3(b) and Tables 3 (part a) and 4 (part a). These tests were performed using the ECI method. Minimum, maximum, mean, and median values of JNDs and ΔE^{CIE94} units are presented for the three least-squares regressions. According to these simulations, SkyRadLS and SkyRadSPPLS have significantly better performance than the MaxIgnSPPLS. For SkyRadLS and SkyRadSPPLS, mean and median values are below 0.1 JND, while for MaxIgnSPPLS the same values are close to 0.2 JND. In all cases, the largest portion of the set is kept below 0.25 JND, while all of the samples produce errors below 0.5 JNDs.

Tables 3 (part b) and 4 (part b) present the standard deviations of all the pixels in an image for every radiance sample. Then the minimum, maximum, mean, and median values of all the 912 standard deviations are estimated. Although noise may have a pronounced effect on individual image elements, the averaging of these elements can suppress noise. However, during our simulations we observed noise originating errors (for a single pixel of a single measurement) up to 1.8 JNDs.

Tables 5 and 6 were constructed similarly to Tables 3 and 4. This time the colorimetric performance of the various demosaicking algorithms was tested using the SkyRadSPPLS transformation. According to Tables 5 (part a) and 6 (part a), the colorimetric performance of all interpolation methods is almost identical. However, there is significant difference between the noise originating errors [Tables 5 (part b) and 6 (part b)]. The SHTI method is more accurate with a mean ΔE^{CIE94} error of 0.23 units. The ECI and the BI methods resulted in 13 and 26% increases of the mean error values [Table 6 (part b)].

4.2 *Evaluation of the Noise Propagation Equations*

In this section, the DCM is used, while introducing the same amount of signal (electrons) to all three sensor classes and subsequently raising the signal level. The output of the DCM is uniform, CIE XYZ images (no vignetting), of 30

Table 3 Colorimetric performance (a) and noise originating errors (b)—Euclidean distance.

(a) Colorimetric Performance—Euclidean Distance

BG39 NIR Glass	<1/10 JND (%)	<1/4 JND (%)	<1/2 JND (%)	Min	Max	Mean	Median
MaxIgnSPPLS	26.0	57.8	100	0.008	0.45	0.200	0.219
SkyRadLS	81.5	100	100	0.004	0.24	0.067	0.063
SkyRadSPPLS	90.57	99.34	100	0.003	0.34	0.057	0.050

(b) Noise Originating Errors—Euclidean Distance

	Min JND	Max JND	Mean JND	Median JND
MaxIgnSPPLS	0.13	0.22	0.17	0.18
SkyRadLS	0.14	0.23	0.18	0.18
SkyRadSPPLS	0.13	0.22	0.17	0.17

In Part (a), percentages of the samples with ΔE^*_{ab} less than 0.1, 0.25, and 0.5 JNDs, for the ECI method and for various color space transformations.

In part (b), min, max, mean, and median standard deviations are estimated from all samples.

×40 pixels. The standard deviations and signal-to-noise ratios (SNRs) of these images are calculated and compared against the theoretical noise analysis of the system. To study the noise performance of the DCM, we used the PTC Eq. (11) and compensated the results for the ADC stage. To study the BI demosaicking method, we used Eqs. (14) and (39). For the SHTI method, we used Eqs. (15) and (48). Performance of the ECI method was evaluated using Eqs. (16) and (17). Finally, Eqs. (19) and (20) were used to estimate the magnitude of the output errors due to the color space transformations. Table 7 summarizes the statistical evaluation of the error propagation equations, for the three demosaicking methods. The performance of the noise propagation equations is studied at all stages of the DCM (the noise module, the interpolation, and the color transformation). At each evaluation stage, all noise propagation equations from the preceding stages also participate.

4.2.1 *Evaluation of BI noise propagation equations*

Figure 4 displays the noise output of the DCM against the error propagation equations for the case of BI and the SkyRadSPPLS regression. Calculations were performed using Eq. (14). However, similar results are obtained when

Table 4 Colorimetric performance (a) and noise originating errors (b)—CIE94 color difference.

(a) Colorimetric performance—CIE94 color difference.

BG39 NIR Glass	<1/10 (%)	<1/4 (%)	<1/2 (%)	Min	Max	Mean	Median
MaxIgnSPPLS	22.0	45.3	97.7	0.006	0.844	0.268	0.298
SkyRadLS	65.2	98.2	100	0.006	0.36	0.090	0.080
SkyRadSPPLS	73.46	99.01	100	0.003	0.49	0.079	0.069

(b) Noise originating errors—CIE94 color difference.

	Min	Max	Mean	Median
MaxIgnSPPLS	0.18	0.42	0.26	0.26
SkyRadLS	0.17	0.39	0.27	0.28
SkyRadSPPLS	0.15	0.38	0.26	0.27

In part (a), percentages of the samples with $\Delta E^{\mathrm{CIE94}}$ less than 0.1, 0.25, and 0.5 of color difference units, for the ECI method and for various color space transformations.

In part (b), min, max, mean, and median standard deviations are estimated from all samples.

Table 5 Demosaicking colorimetric performance (a) and demosaicking noise originating errors (b)—Euclidean distance.

(a) Demosaicking Colorimetric Performance—Euclidean Distance

BG39 NIR Glass	<1/10 JND (%)	<1/4 JND (%)	<1/2 JND (%)	Min	Max	Mean	Median
BI	90.67	99.45	100	0.006	0.33	0.058	0.051
SHTI	91.23	99.45	100	0.004	0.30	0.058	0.053
ECI	90.57	99.34	100	0.003	0.34	0.057	0.050

(b) Demosaicking Noise Originating Errors—Euclidean Distance

	Min JND	Max JND	Mean JND	Median JND
BI	0.16	0.25	0.20	0.20
SHTI	0.12	0.20	0.15	0.15
ECI	0.13	0.22	0.17	0.17

In part (a), percentages of the samples with ΔE^*_{ab} less than 0.1, 0.25, and 0.5 JNDs, for the SkyRad-SPPLS transformation and for various demosaicking methods.

In part (b), min, max, mean, and median standard deviations are estimated from all samples.

we applied the approximation of Eqs. (39). According to Table 7, the agreement between the DCM operation and the noise analysis is excellent.

Theoretical and simulated XYZ SNRs for the particular configuration of the imaging pipeline were also calculated. The abrupt scaling of the SNRs is due to the quantization of the signal. The maximum SNR of the sensor (for a 40 k electrons signal with the associated shot noise) is about 46 dB. However, the DCM output exhibits maximum SNRs of 44.2, 43.3, and 40.5 dB for the X, Y, and Z channels, respectively. SNR values are not the same for all channels. The Z channel of the CIE XYZ tristimulus has the lower SNRs. Since, in many cases, sky radiance is dominated by the blue portions of the spectrum, higher SNRs would be desirable. The main reason for this behavior is the data transformation to CIE XYZ color space. An initially spherical error cloud tends to be elongated in one or more directions,[52] creating the different SNR curves in Fig. 4 for the same initial signal. Closer investigation of all the regression methods used in our study reveals that this is the general behavior of the DCM.

Table 6 Demosaicking colorimetric performance (a) and demosaicking noise originating errors (b)—CIE94 color difference.

(a) Demosaicking Colorimetric Performance—CIE94 Color Difference

BG39 NIR Glass	<1/10 (%)	<1/4 (%)	<1/2 (%)	Min	Max	Mean	Median
BI	75.90	98.90	100	0.004	0.48	0.078	0.068
SHTI	75.48	99.01	100	0.006	0.45	0.079	0.071
ECI	73.46	99.01	100	0.003	0.49	0.079	0.069

(b) Demosaicking Noise Originating Errors—CIE94 Color Difference

	Min	Max	Mean	Median
BI	0.18	0.55	0.29	0.28
SHTI	0.16	0.36	0.22	0.22
ECI	0.15	0.38	0.26	0.27

In part (a), percentages of the samples with $\Delta E^{\mathrm{CIE94}}$ less than 0.1, 0.25, and 0.5 of color difference units, for the SkyRadSPPLS transformation and for various demosaicking methods.

In part (b), min, max, mean, and median standard deviations are estimated from all samples.

Table 7 Evaluation of the error propagation equations.

DCM Stage and Participating Noise Propagation Equations	Channel	Mean of Residuals $\mu_R=\frac{1}{n}\sum_{i=1}^{n}(O_i-P_i)$ /(Range of observed values)	Slope $m=\frac{\sum_{i=1}^{n}O_iP_i-(1/n)\sum_{i=1}^{n}O_i\sum_{i=1}^{n}P_i}{\sum_{i=1}^{n}O_i^2-(1/n)(\sum_{i=1}^{n}O_i)^2}$	Correlation Coefficient $\rho=\frac{ms_o}{s_p}$
PTC, (11)	R-$G-B$	0.010	1.02	0.98
BI, (11) and (14)	R-B	0.006	1.03	0.98
	G	0.010	1.04	0.98
BI, (11) and (39)	R-B	0.001	1.02	0.98
	G	0.010	1.04	0.98
SkyRadSPPLS, (11), (14), and (19)	X	0.008	1.05	0.98
	Y	0.006	1.04	0.98
	Z	−0.002	1.03	0.97
SkyRadSPPLS, (11), (39), and (19)	X	0.003	1.03	0.98
	Y	0.004	1.02	0.98
	Z	−0.008	1.00	0.97
SHTI, (11) and (15)	R-B	0.012	1.15	0.97
	G		Same as BI green channel	
SHTI, (11) and (48)	R-B	−0.045	0.78	0.97
	G		Same as BI green channel	
SkyRadSPPLS, (11), (15), and (19)	X	0.003	1.10	0.97
	Y	−0.024	0.97	0.97
	Z	0.039	1.27	0.97
SkyRadSPPLS, (11), (48), and (19)	X	−0.053	0.76	0.97
	Y	−0.062	0.77	0.97
	Z	0.039	0.87	0.98
ECI, (11), (16), and (17)	R-B	0.004	0.98	0.97
	G	0.012	1.03	0.97
SkyRadSPPLS, (11), (16), (17), and (20)	X	0.004	0.99	0.97
	Y	0.008	1.01	0.97
	Z	−0.007	0.97	0.97
Skylight samples (11), (16), (17), and (20)	X	0.062	1.10	0.99
	Y	0.030	1.03	0.99
	Z	−0.007	0.95	0.98

Evaluation of the error propagation equations estimated at various stages of the DCM. Three cases are presented (i.e., BI, SHTI, and ECI with luminance channel biased). The last rows present the equations evaluation for ECI and MaxIgnSPPLS for all MODTRAN generated samples. Observed values (Q_i) are derived from DCM operation while predicted values are calculated using the noise propagation equations. Also, s_o and s_p are the standard deviations of observed and predicted noise.

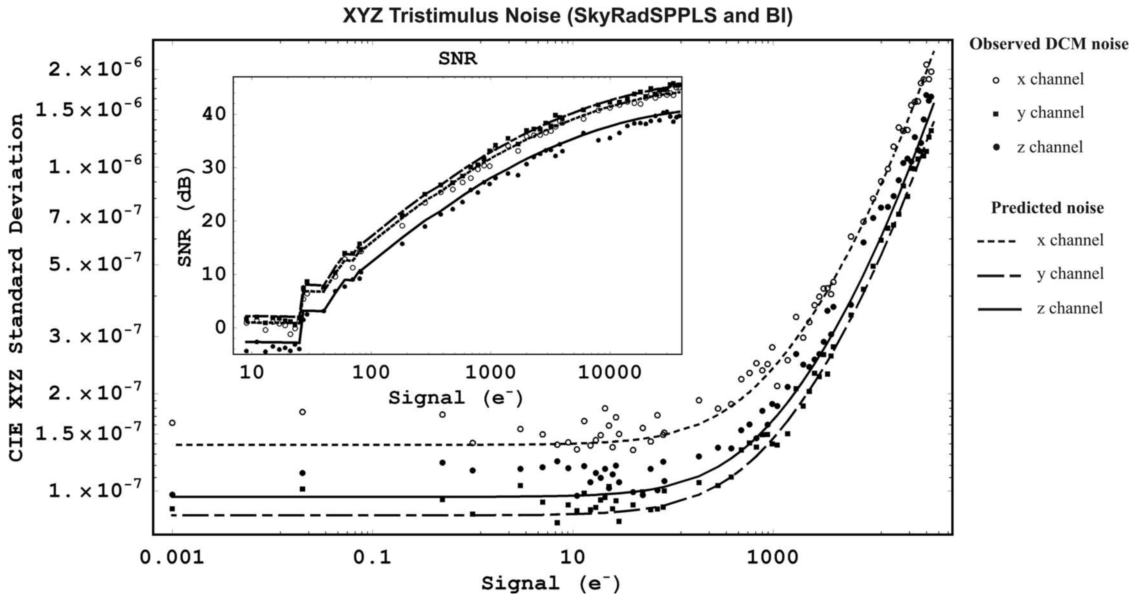

Fig. 4 Simulated camera operation noise results and SNR ratios. CIE *XYZ* predicted noise was calculated using Eqs. (11), (14), and (19). Simulations were performed using the SkyRadSPPLS transformation and the BI method.

4.2.2 *Evaluation of SHTI noise propagation equations*

Figure 5 displays the noise output of the DCM against the error propagation equations for the case of the SHTI and the SkyRadSPPLS transformation. Application of Eqs. (15) or (48) gives poorer results when compared to the DCM operation. According to Sec. 3.5, we derived Eqs. (15) and (48) assuming that all participating variables during the execution of the SHTI algorithm are statistically independent. Although SHTI exhibits fewer correlations if compared to the ECI method, the preceding assumption is not always correct. Despite this problem, both Eqs. (15) and (48) are relatively accurate and successfully describe the noise propagation of SHTI (Table 7). The DCM operation with SHTI exhibits maximum SNRs of 42.0, 43.4, and 39.5 dB for the X, Y, and Z channels, respectively.

Another problem originates from the nature of the SHTI algorithm itself. According to Eq. (15), the amount of noise injected from the green channel depends on the ratio of chrominance to luminance ($\bar{x}/\bar{g}$). A value larger than 1 results in amplification of the injected G channel noise. This is likely to create severe noise artifacts in the final image in

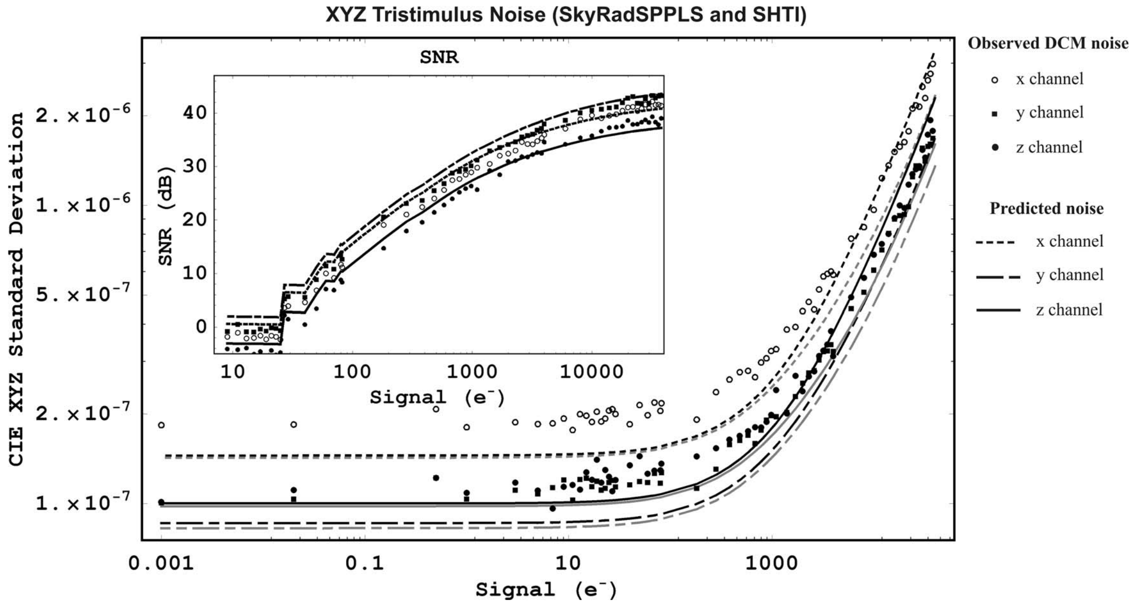

Fig. 5 Simulated camera operation noise results and SNRs. CIE *XYZ* predicted noise was calculated using Eqs. (11), (14), (15), and (19). Simulations were performed using the SkyRadSPPLS transformation and the SHTI method. Gray lines are plotted using the approximate Eqs. (11), (48), and (19).

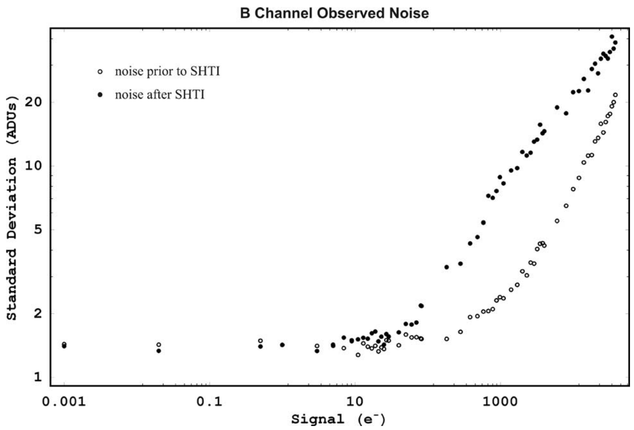

Fig. 6 Simulated DCM noise output for the *B* channel. The plot presents the noise output prior to SHTI and after the demosaicking procedure. DCM input was adjusted to raise higher signal levels for the *B* channel and lower signal levels for the *G* channel.

the case of very high chrominance and very low luminance values. To prove our point, we performed simulations introducing unequal amounts of signal to the *RGB* channels. During these simulations the *B* channel signal was always 20 times higher than the *G* channel signal level ($B/G = 20$). We also varied the *B* channel signal level from 0 up to 40 k electrons. Results of the *B* noise levels before and after the SHTI demosaicking algorithm are presented in Fig. 6. According to Fig. 6, for an input signal level of 1 k electrons, the SHTI algorithm produced noise levels that would be normally expected at an input signal level of 10 k electrons. We believe that implementation of SHTI in a real single-sensor camera can be potentially problematic.

4.2.3 *Evaluation of ECI noise propagation equations*

To predict the noise output of the DCM using Eqs. (16) and (17), we estimated the correct values for the r_1, r_2, r_1', r_2', and r_3 correlation coefficients. We also used Eq. (20) instead of Eq. (19), since color channels are statistically correlated after the ECI demosaicking stage. Since correlation coefficients are also present in Eq. (20), we estimated the correct r_{rg}, r_{rb}, and r_{gb} values. The correlation coefficients of Eqs. (16) and (17) were estimated according to Eq. (50). For this purpose, we performed subsequent runs of the DCM and we calculated the variance and covariance of the various channels and domains that participate during the ECI algorithm execution. The correlation coefficients of Eq. (20) were estimated in a similar manner. Calculated values of the various coefficients are presented in Table 8. Since the values of the correlation coefficients depend on the relative magnitude of the color channels, we consider two cases.

In the first case, the correlation coefficients were determined for the same amount of signal in the *RGB* channels. Figure 7 displays the noise output of the DCM against the error propagation equations for the case of ECI and the SkyRadSPPLS transformation. As shown in this figure, the introduction of covariances in the derivation of the noise propagation equations gave excellent results (Table 7). The DCM operation with ECI exhibits maximum SNRs of 41.7, 42.2, and 40.6 dB for the *X*, *Y*, and *Z* channels, respectively.

In the second case, we calculated the mean value of each coefficient for all 912 skylight samples. Since each sample has a unique set of correlation coefficients the estimated noise using Eqs. (16), (17), and (20) is only approximate. The coefficients presented in Table 8 represent the mean values of the 912 sets of coefficients. According to Fig. 8 and Table 7 (last rows), the predicted performance is similar to the observed performance. This simplifies the problem of estimating the noise propagation for skylight samples in the future, since the described coefficients can be used.

5 Conclusion

The DCM described in this study has many applications. Extended parameterization of the CCD model enables the simulation of the colorimetric and noise performance of various CCD sensors, as embedded in the imaging pipeline, before hardware implementation. Since the model input of the DCM is spectral radiance, it can be used to estimate the color output of various atmospheric radiation models, like MODTRAN, or it can be used with measured sky radiance data.

Table 8 Correlation coefficients for the ECI error propagation equations (a) and for SkyRadSPPLS (b).

(a) Correlation Coefficients for the ECI Error Propagation Equations

Color Channel	*R*		*G*			*B*		
Correlation coefficients	r_1	r_2	r_1'	r_2'	r_3	r_1'	r_2'	r_3
Equal *RGB* signal	−0.65	−0.65	0.41	0.41	0.64	0.41	0.41	0.64
MODTRAN data	−0.44	−0.73	0.57	0.45	0.40	0.31	0.32	0.63

(b) Correlation Coefficients for SkyRadSPPLS

Correlation coefficients	r_{rg}	r_{rb}	r_{gb}
Equal *RGB* signal	0.74	0.64	0.74
MODTRAN data	0.81	0.68	0.68

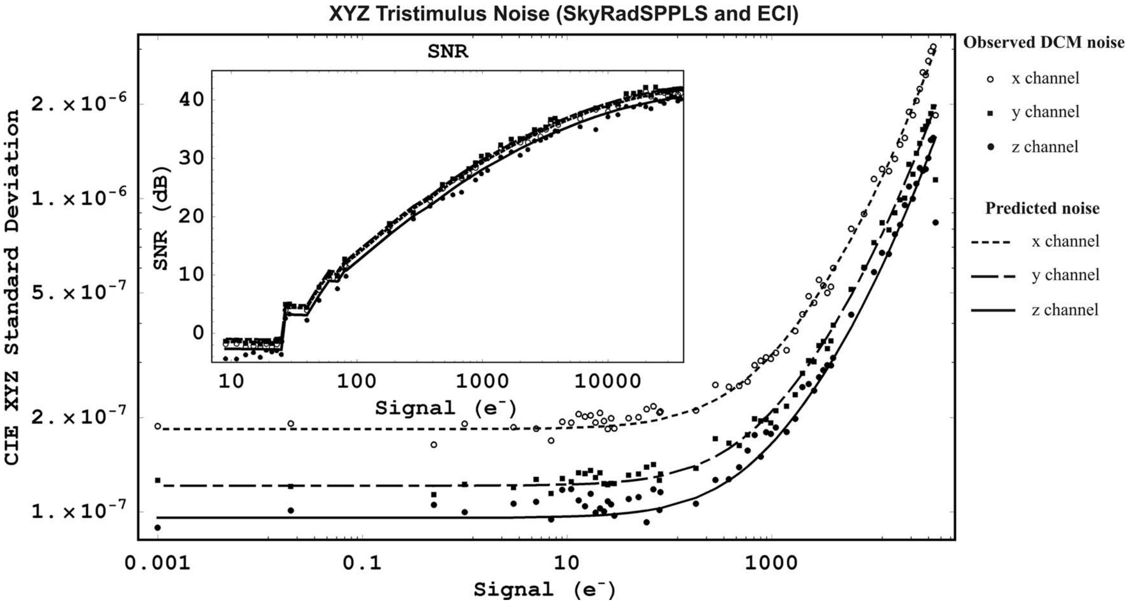

Fig. 7 Simulated camera operation noise results and SNRs. CIE *XYZ* predicted noise was estimated using Eqs. (11), (16), (17), and (20). Simulations were performed using SkyRadSPPLS transformation and the ECI method.

In this study, we derived a set of error propagation equations, such as Eqs. (11), (14), and (15). These equations form a separate noise model apart from the DCM. This "new" model facilitates the investigation of the noise performance of a digital imaging pipeline from the CCD-generated electrons up to the *XYZ* tristimulus values. Although the DCM with the noise module gives more accurate results, it is computationally time consuming and a much more complicated procedure, compared to the straightforward implementation of the noise equations.

Using the same analysis, we investigated a different approach of demosaicking algorithms. Since such methods become more complicated as they progress, little attention is paid to the noise performance. When CFA cameras are used as colorimeters, the overall accuracy of the system might be degraded due to poor choice of the demosaicking method.

Taking into account the color output performance of Sec. 4.1, both SkyRadLS and SkyRadSPPLS methods gave accurate measurements of skylight color. However, to measure color accurately, we must either use a low resolution CCD camera equipped with narrow field of view (FOV) lenses, or a high-resolution CCD camera with wider FOV lenses. Both setups will produce sky images that contain uniform flat-field segments. This enables the estimation of the mean camera response for various sky positions. Since cloudless sky during daytime is a very bright target, the signal of the sensor will be high and the camera will work in the shot-noise-limited region. Cooling the CCD will not improve measurement accuracy, since BDC is small compared to SSN. To increase color recovery accuracy from a single pixel, or to reduce the number of averaged pixels, a sensor with an increased photosite area, or a higher saturation signal should be used.

In Section 4.2, we tested the noise equations against the noise performance of the imaging pipeline and we found that there were consistent with the noise output of the DCM. Closer investigation of Eq. (15) made apparent a

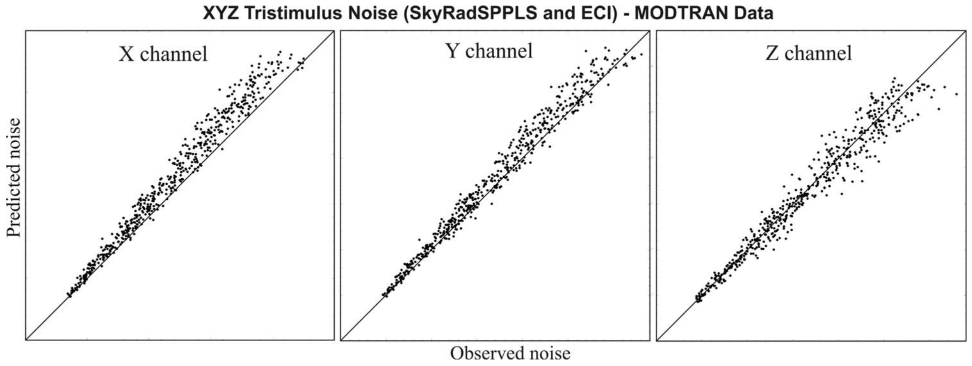

Fig. 8 Simulated camera operation noise results for 912 skylight samples. CIE *XYZ* observed and predicted noise performances for the ECI method and the SkyRadSPPLS transformation. Solid line is the $x = y$. Axis units are arbitrary

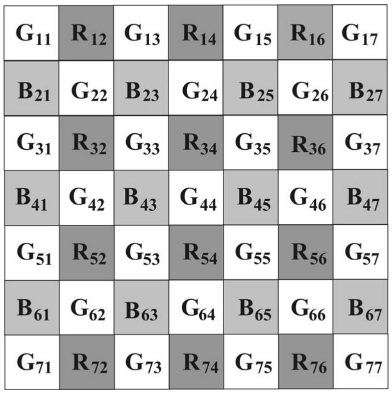

G_{11}	R_{12}	G_{13}	R_{14}	G_{15}	R_{16}	G_{17}
B_{21}	G_{22}	B_{23}	G_{24}	B_{25}	G_{26}	B_{27}
G_{31}	R_{32}	G_{33}	R_{34}	G_{35}	R_{36}	G_{37}
B_{41}	G_{42}	B_{43}	G_{44}	B_{45}	G_{46}	B_{47}
G_{51}	R_{52}	G_{53}	R_{54}	G_{55}	R_{56}	G_{57}
B_{61}	G_{62}	B_{63}	G_{64}	B_{65}	G_{66}	B_{67}
G_{71}	R_{72}	G_{73}	R_{74}	G_{75}	R_{76}	G_{77}

Fig. 9 Bayer CFA pattern.

drawback of SHTI. In the worst case scenario of an image with high chrominance and low luminance, the noise of the CFA may multiply and severely deteriorate image quality. For this reason, the SHTI method is unsuitable for our purpose.

6 Appendix A: Description of the Demosaicking Methods

6.1 *BI*

Consider an array of pixels as shown in Fig. 9. At position 4,3 only a B pixel is available, that is; $B_{4,3}$. To estimate the G value, $G_{4,3}$, we use the neighboring pixels, $G_{3,3}$, $G_{4,4}$, $G_{5,3}$, and $G_{4,2}$. The interpolated value is calculated as $G_{3,4}=(G_{3,3}+G_{4,4}+G_{5,3}+G_{4,2})/4$. To determine $R_{4,3}$ we calculated $R_{4,3}=(R_{3,2}+R_{3,4}+R_{5,4}+R_{5,2})/4$. Interpolation for the rest of the pixels is carried out in the same way.

6.2 *SHTI*

In the case of SHTI, the R and B pixels are assigned to be the chrominance channels and G to be the luminance channel. Hue is defined as the ratios R/G and B/G. Interpolation is carried out in the hue domain. The interpolation of G pixels is the same as BI.

For the case of B pixels there are two subcases. For the estimation of a B pixel at a G position the adjacent blue pixels are placed horizontally or vertically of the G pixel. For the case of $B_{4,4}$, this is given by $B_{4,4}=G_{4,4}(B_{4,3}/G_{4,3}+B_{4,5}/G_{4,5})/2$. For the estimation of a B pixel at an R position, all adjacent pixels are placed diagonally of the R pixel. The value of $B_{3,4}$ is estimated by $B_{3,4}=G_{3,4}(B_{2,3}/G_{2,3}+B_{2,5}/G_{2,5}+B_{4,5}/G_{4,5}+B_{4,3}/G_{4,3})/4$. The interpolation of the R pixels is similar.

6.3 *ECI*

ECI exploits the correlation between RGB channels. This method is similar to SHTI but less complex. We define K_R and K_B as $G-R$ and $G-B$, respectively. Interpolation is carried out in the K_R and K_B domains, while this time the G channel interpolation uses information from the R and B channels.

To estimate a G value at a R position, such as $G_{3,4}$, we calculate all K_R values at the neighboring G pixels. We estimated $K_{R2,4}$ as $K_{R2,4}=G_{2,4}-(R_{1,4}-R_{3,4})/2$, and calculated $K_{R3,5}$, $K_{R4,4}$, and $K_{R3,3}$ in the same way. The G pixel is calculated as $G_{3,4}=R_{3,4}+(K_{R2,4}+K_{R3,5}+K_{R4,4}+K_{R3,3})/4$. Estimation of a G value at a B position is performed in the K_B domain.

To interpolate an R pixel at a G position, such as $R_{4,4}$, we always interpolate in the K_R domain. The R value is estimated as $R_{4,4}=G_{4,4}-(K_{R3,4}+K_{R5,4})/2$. A B pixel interpolation at a R position, such as $B_{5,4}$, is always carried out in the K_B domain. In that case, $B_{5,4}$ is calculated as $B_{5,4}=G_{5,4}-(K_{B4,5}+K_{B6,5}+K_{B6,3}+K_{B4,3})/4$. This time, $G_{5,4}$ is an interpolated G value.

7 Appendix B: Noise Propagation Equations of the Noise Module

Let z be an arbitrary function of $a,b,\ldots$ and variables $z=f(a,b,\ldots)$. Let $\Delta a,\Delta b,\ldots$ be the noise elements of these variables approximated by the standard deviations. The final error of z is given by[42]:

$$(\Delta z)^2=\left(\frac{\partial z}{\partial a}\Delta a\right)^2+\left(\frac{\partial z}{\partial b}\Delta b\right)^2+\cdots. \qquad (21)$$

It is assumed that the variables are statistically independent and the standard deviations are small[42] compared to a and b. Otherwise, higher order terms must be taken into account.[51] Most of the times Eq. (21) takes the form of a simple sum of squares.

The mean values of matrices $\mathbf{M}_{\mathrm{DCSN}}$, $\mathbf{M}_{\mathrm{DCNU}}$, $\mathbf{M}_{\mathrm{SSN}}$, $\mathbf{M}_{\mathrm{PRNU}}$, and $\mathbf{M}_{\mathrm{RON}}$ are denoted as $\bar{m}^{\mathrm{DCSN}}$, $\bar{m}^{\mathrm{DCNU}}$, $\bar{m}^{\mathrm{SSN}}$, $\bar{m}^{\mathrm{PRNU}}$, and $\bar{m}^{\mathrm{RON}}$, respectively. These mean values are

$$\bar{m}^{\mathrm{DCSN}}=Q_{\mathrm{DC}}, \qquad (22a)$$

$$\bar{m}^{\mathrm{DCNU}}=1, \qquad (22b)$$

$$\bar{m}^{\mathrm{SSN}}=\rho^k, \qquad (22c)$$

$$\bar{m}^{\mathrm{PRNU}}=1, \qquad (22d)$$

$$\bar{m}^{\mathrm{RON}}=0, \qquad (22e)$$

where ρ^k is the electron signal due to incident light independent of position of the photosite (no vignetting). Keeping in mind that all operators of Eq. (10) are elementwise, and by implementing Eq. (21) on the product $\mathbf{M}_{\mathrm{DCSN}}*\mathbf{M}_{\mathrm{DCNU}}=\|u_{i,j}\|=\|m_{i,j}^{\mathrm{DCSN}}\cdot m_{i,j}^{\mathrm{DCNU}}\|$, the variance is estimated:

$$\left(\frac{\Delta u}{\bar{u}}\right)^2=\left(\frac{\sigma_{\mathrm{DCSN}}}{Q_{\mathrm{DC}}}\right)^2+\frac{(\sigma_{\mathrm{DCNU}})^2}{1}. \qquad (23)$$

Since $\mathbf{M}_{\mathrm{DCNU}}$ randomly rescales the $\mathbf{M}_{\mathrm{DCSN}}$ array (element by element) and because of Eq. (22b) the mean value of $\mathbf{M}_{\mathrm{DCSN}}$ is left unchanged. Taking into account Eq. (8a) the latter equation is simplified:

$$(\Delta u)^2=Q_{\mathrm{DC}}+(Q_{\mathrm{DC}}\sigma_{\mathrm{DCNU}})^2. \qquad (24)$$

For the case of the signal matrix product $\mathbf{M}_{\mathrm{SSN}}*\mathbf{M}_{\mathrm{PRNU}}=\|v_{i,j}\|=\|m_{i,j}^{\mathrm{SSNP}}\cdot m_{i,j}^{\mathrm{PRNU}}\|$, derivation of variance $(\Delta v^k)^2$ for each color channel is similar to Eq. (24):

$$(\Delta v^k)^2 = \rho^k + (\rho^k \sigma_{\mathrm{DCNU}})^2. \tag{25}$$

Taking into account Eqs. (21), (24), and (25) and the standard deviation of readout noise σ_{RON} we calculate the noise equation:

$$(\Delta m^k)^2 = Q_{\mathrm{DC}} + \rho^k + (Q_{\mathrm{DC}}\sigma_{\mathrm{DCNU}})^2 + (\rho^k \sigma_{\mathrm{PRNU}})^2 + (\sigma_{\mathrm{RON}})^2. \tag{26}$$

8 Appendix C: Noise Propagation of BI

Derivations of the following equations are valid only for flat-field portions of images. Let σ_o and σ_{demos} be the standard deviations of the initial and the interpolated data sets x_i. The data populations (number of pixels) are n and n', respectively. Since k new elements are added, $n' > n$ and $k = n' - n$. The new data consist of the old values and the new demosaicked ones: $x_1, x_2, \ldots, x_{n-1}, x_n, \ldots, x_{n'-1}, x_{n'}$. Variances for both data sets are given by

$$(\sigma_o)^2 = \frac{1}{n-1}\sum_{i=1}^{n}(x_i - \bar{x})^2, \tag{27}$$

$$(\sigma_{\mathrm{demos}})^2 = \frac{1}{n'-1}\sum_{i=1}^{n'}(x_i - \bar{x})^2, \tag{28}$$

where $\bar{x}$ is the mean value. Since data are interpolated, both sets have the same mean value $\bar{x}$. Equation (28) can be restated by discriminating the old from the new values:

$$(\sigma_{\mathrm{demos}})^2 = \frac{1}{n'-1}\left[\sum_{i=1}^{n}(x_i - \bar{x})^2 + \sum_{i=n+1}^{n'}(x_i - \bar{x})^2\right]. \tag{29}$$

Equation (29) is rewritten taking into account the k new elements added, of $(\sigma_{\mathrm{add}})^2$ variance:

$$(\sigma_{\mathrm{demos}})^2 = \left(1 - \frac{k}{n'-1}\right)(\sigma_o)^2 + \frac{k-1}{n'-1}(\sigma_{\mathrm{add}})^2, \tag{30}$$

$$(\sigma_{\mathrm{add}})^2 = \frac{1}{k-1}\sum_{i=1}^{k}(x_i - \bar{x})^2. \tag{31}$$

For a new element x_{add} with m neighbors, interpolation can generally be described by

$$x_{\mathrm{add}} = \frac{1}{m}\sum_{1}^{m} x_i. \tag{32}$$

Using Eq. (32) and taking into account Eq. (21), the missing variance $(\sigma_{\mathrm{add}})^2$ is estimated:

$$\begin{aligned}(\sigma_{\mathrm{add}})^2 &= \left(\frac{1}{m}\right)^2(\sigma_1)^2 + \left(\frac{1}{m}\right)^2(\sigma_2)^2 + \cdots + \frac{1}{m}(\sigma_m)^2 \\ &= \left(\frac{1}{m}\right)^2\sum_{i=1}^{m}(\sigma_i)^2,\end{aligned} \tag{33}$$

where $(\sigma_1)^2, (\sigma_2)^2, \ldots, (\sigma_m)^2$ are the variances of the elements taking part in the interpolation. These errors depend on the variance of the initial set so they must all be equal to $(\sigma_o)^2$. Variance $(\sigma_{\mathrm{add}})^2$ becomes

$$(\sigma_{\mathrm{add}})^2 = \frac{1}{m}(\sigma_o)^2. \tag{34}$$

Substituting Eq. (34) into Eq. (30), the error dispersion of bilinear interpolation can be calculated:

$$\sigma_{\mathrm{demos}} = \left[\left(1 - \frac{k}{n'-1}\right)(\sigma_o)^2 + \frac{k-1}{n'-1}\frac{1}{m}(\sigma_o)^2\right]^{1/2}. \tag{35}$$

The previous equation can be further simplified. If we substitute $k = n' - n$ in Eq. (35), we find

$$\sigma_{\mathrm{demos}} = \sigma_o\left(\frac{n-1}{n'-1} + \frac{1}{m}\frac{n'-n-1}{n'-1}\right)^{1/2}. \tag{36}$$

For the Bayer CFA, the number of green pixels is roughly twice the number of one chrominance (red or blue) pixels. Let p be the population of one chrominance pixels. The total number of pixels is $n' = 2p + p + p = 4p$. For the green plane, the interpolation m value must be substituted from its mean, since the number of neighbors is not constant across the CFA. The magnitude of m tends to a value of 4 as the CFA becomes more populated. For that case, $(n = 2p,\ m = 4)$, Eq. (36) becomes

$$\sigma_{\mathrm{demos}}^{g} = \sigma_o^{g}\left(\frac{5 - 10p}{4 - 16p}\right)^{1/2}. \tag{37}$$

By simulating the Bayer CFA construction we found out that for the red or blue plane interpolation the mean value of m tends to 2.66. In this case, $(n = p,\ m = 2.66)$:

$$\sigma_{\mathrm{demos}}^{r,b} = \sigma_o^{r,b}\left(\frac{3.66 - 5.66p}{2.66 - 10.64p}\right)^{1/2}. \tag{38}$$

For a large number of photosites, the preceding equations are approximated by

$$\sigma_{\mathrm{demos}}^{r,b} = \sigma_o^{r,b}\sqrt{0.53} \tag{39a}$$

$$\sigma_{\mathrm{demos}}^{g} = \sigma_o^{g}\sqrt{5/8}. \tag{39b}$$

The preceding results indicate that during bilinear interpolation, the noise is decreased by a constant of 0.73 for the red or blue color planes and by 0.79 for the green regardless of the CFA elements magnitude.

9 Appendix D: Noise Propagation of SHTI

When SHTI is utilized, the green plane is bilinear interpolated. The noise of the interpolated green channel can be estimated by Eq. (36) or Eq. (39). Let $\bar{x}$ be the mean value of the remaining colors, red or blue, while $\bar{g}$ is the mean value of BI green. Let n be the CFA population of one chrominance interpolated plain, v be the number of green pixels, and w be the other chrominance pixels. The total population is $n' = n + v + w$. Since the SHTI procedure depends on whether or not we calculate a chrominance value at a luminance point, we must break the variance of Eq. (28) into three discrete sums. The noise of the demosaicked chrominance channels will be

$$(\sigma^{x}_{\mathrm{demos}})^2=\frac{1}{n'-1}\left[\sum_{i=1}^{n}(x_i-\bar{x})^2+\sum_{i=1}^{v}(x_i-\bar{x})^2+\sum_{i=1}^{w}(x_i-\bar{x})^2\right]. \tag{40}$$

Let σ^x_o be the original noise of a particular CFA color (red or blue). Let $\sigma^{x\rightarrow g}_{\mathrm{add}}$ be the added error from the interpolation of a chrominance value at a green position ($x\rightarrow g$, e.g., blue at a green position). Also $\sigma^{x\rightarrow c}_{\mathrm{add}}$ is the error from interpolation at the remaining chrominance position ($x\rightarrow c$, e.g., blue at a red position). We must discriminate the two cases, since a different number of neighbors participates at each one. The final error can be restated as

$$(\sigma^{x}_{\mathrm{demos}})^2=\frac{n-1}{n'-1}(\sigma^x_o)^2+\frac{v-1}{n'-1}(\sigma^{x\rightarrow g}_{\mathrm{add}})^2+\frac{w-1}{n'-1}(\sigma^{x\rightarrow c}_{\mathrm{add}})^2. \tag{41}$$

Now, we estimate the added noise $\sigma^{x\rightarrow g,c}_{\mathrm{add}}$ for both cases. By following the steps of the algorithm, and utilizing Eqs. (21) and (34), the added noise is estimated:

$$(\sigma^{x\rightarrow g,c}_{\mathrm{add}})^2=\frac{1}{m}[(\sigma^x_o)^2+(\bar{x}/\bar{g})^2(m+1)(\sigma^g_{\mathrm{demos}})^2]. \tag{42}$$

The last equation incorporates the transformation of data into hue ratios, the averaging of ratios, and the calculation of the interpolated chrominance plus the final restoration of data back to chrominance values. For the case of a chrominance value at a green position ($m=2$) Eq. (42) becomes:

$$(\sigma^{x\rightarrow g}_{\mathrm{add}})^2=\frac{1}{2}(\sigma^x_o)^2+\frac{3}{2}(\bar{x}/\bar{g})^2(\sigma^g_{\mathrm{demos}})^2, \tag{43}$$

and for all other cases ($m=4$),

$$(\sigma^{x\rightarrow c}_{\mathrm{add}})^2=\frac{1}{4}(\sigma^x_o)^2+\frac{5}{4}(\bar{x}/\bar{g})^2(\sigma^g_{\mathrm{demos}})^2. \tag{44}$$

By substitution of Eqs. (43) and (44) into Eq. (41), we calculate the variance of noise $(\sigma^x_{\mathrm{demos}})^2$ for the demosaicked chrominance channels:

$$(\sigma^{x}_{\mathrm{demos}})^2=\frac{1}{4(n'-1)}\left[(4n+2v+w-7)(\sigma^x_\sigma)^2+(6v+5w-11)\left(\frac{\bar{x}}{\bar{g}}\right)^2(\sigma^g_{\mathrm{demos}})^2\right]. \tag{45}$$

As described in Appendix C, for $n'=4p$, $v=2p$, and $n=w=p$. Thus, Eq. (45) can be rewritten as

$$(\sigma^{x}_{\mathrm{demos}})^2=\frac{1}{16p-4}\left[(9p-7)(\sigma^x_o)^2+(17p-11)\left(\frac{\bar{x}}{\bar{g}}\right)^2(\sigma^g_{\mathrm{demos}})^2\right]. \tag{46}$$

For large values of p the preceding equation is simplified:

$$\sigma^{x}_{\mathrm{demos}}=\frac{1}{4}\left[9(\sigma^x_o)^2+17\left(\frac{\bar{x}}{\bar{g}}\right)^2(\sigma^g_{\mathrm{demos}})^2\right]^{1/2}. \tag{47}$$

For the case of $\bar{g}\gg\bar{x}$, Eq. (47) can be further simplified:

$$\sigma^{x}_{\mathrm{demos}}=\frac{3}{4}\sigma^x_o=0.75\sigma^x_o. \tag{48}$$

10 Appendix E: Noise Propagation of ECI

The use of Eq. (21) requires that all variables are statistically independent. This does not apply for the ECI method. Let z be an arbitrary function of $x_1,x_2,\ldots,x_k,\ldots,x_n$ variables that are not independent, $z=f(x_1,x_2,\ldots,x_k,\ldots,x_n)$. Let σ_k be the standard deviation of x_k. The variance of z, σ^2_z, is given by

$$\sigma^2_z=\sum_{k=1}^{n}\left(\frac{\partial f}{\partial x_k}\right)^2\sigma^2_{x_k}+2\sum_{k=1}^{n-1}\sum_{l=k+1}^{n}\frac{\partial f}{\partial x_k}\frac{\partial f}{\partial x_l}\sigma(x_k,x_l), \tag{49}$$

where $\sigma(x_k,x_l)$ is the covariance of x_k and x_l. Covariance is related to correlation coefficient $r(x_k,x_l)$ and σ_k and σ_l:

$$\sigma(x_k,x_l)=r(x_k,x_l)\sigma_{x_k}\sigma_{x_l},\quad -1\leqslant r(x_k,x_l)\leqslant+1. \tag{50}$$

This analysis is similar to that performed in Appendices C and D. However, we must consider that certain variables that participate in particular steps of the ECI are statistically correlated. We will estimate first the noise propagation for the green channel. Since interpolation depends on whether a green value at a blue or red pixel is estimated, we start with an equation similar to Eq. (41):

$$(\sigma^{g}_{\mathrm{demos}})^2=\frac{n-1}{n'-1}(\sigma^{g\rightarrow r}_{\mathrm{add}})^2+\frac{v-1}{n'-1}(\sigma^g_o)^2+\frac{w-1}{n'-1}(\sigma^{g\rightarrow b}_{\mathrm{add}})^2. \tag{51}$$

Using Eqs. (49) and (50), the variance of all the interpolated green values at red positions, $(\sigma^{g\rightarrow r}_{\mathrm{add}})^2$, can be estimated:

$$(\sigma^{g\rightarrow r}_{\mathrm{add}})^2=(\sigma^r_o)^2+(\sigma^{K_R}_{\mathrm{add}})^2+2r_1\sigma^r_o\sigma^{K_R}_{\mathrm{add}}, \tag{52}$$

where $(\sigma^{K_R}_{\mathrm{add}})^2$ is the added variance from the calculation of the mean value for the K_R neighbors. The red pixel and the neighboring K_R values are correlated, and r_1 is the correlation coefficient. According to Eq. (32), $(\sigma^{K_R}_{\mathrm{add}})^2$ is estimated as equal to $(\sigma^{K_R}_{\mathrm{add}})^2=(1/4)\sigma^2_{K_R}$, and $\sigma^2_{K_R}$ is the variance of the K_R domain. Since K_R values are calculated from different positions of the green and red array, they are uncorrelated with each other. If we consider the interpolation of the red values in order to estimate the $G-R$ value (K_R) the variance, $(\sigma^{K_R}_{\mathrm{add}})^2$, becomes

$$(\sigma_{\text{add}}^{K_R})^2 = \frac{1}{4}\left[(\sigma_o^g)^2 + \frac{1}{2}(\sigma_o^r)^2\right]. \tag{53}$$

According to Eqs. (53) and (52), $(\sigma_{\text{add}}^{g\to r})^2$ is given by

$$(\sigma_{\text{add}}^{g\to r})^2 = \frac{1}{8}\{9(\sigma_o^r)^2 + 2(\sigma_o^g)^2 + 4\sqrt{2}r_1[2(\sigma_o^g)^2 + (\sigma_o^r)^2]^{1/2}\}. \tag{54a}$$

The derivation of the equation that describes $(\sigma_{\text{add}}^{g\to b})^2$ is similar:

$$(\sigma_{\text{add}}^{g\to b})^2 = \frac{1}{8}\{9(\sigma_o^b)^2 + 2(\sigma_o^g)^2 + 4\sqrt{2}r_2[2(\sigma_o^g)^2 + (\sigma_o^b)^2]^{1/2}\}, \tag{54b}$$

where r_2 is the correlation coefficient between blue values and the K_B domain. We can now estimate the noise propagation equation for the green channel. As described in Appendices C and D, $n'=4p$, $v=2p$, $n=w=p$, and p is very large. Equation (51) becomes

$$(\sigma_{\text{demos}}^g)^2 = \frac{1}{32}\{9(\sigma_o^r)^2 + 20(\sigma_o^g)^2 + 9(\sigma_o^b)^2 + 4\sqrt{2}r_1\sigma_o^r[2(\sigma_o^g)^2 + (\sigma_o^r)^2]^{1/2} + 4\sqrt{2}r_2\sigma_o^b[2(\sigma_o^g)^2 + (\sigma_o^b)^2]^{1/2}\}. \tag{55}$$

If all values are uncorrelated ($r_1=r_2=0$), the preceding equation is simplified:

$$(\sigma_{\text{demos}}^g)^2 = \frac{1}{32}[9(\sigma_o^r)^2 + 20(\sigma_o^g)^2 + 9(\sigma_o^b)^2]. \tag{56}$$

To estimate the variances for the demosaicked red and blue channels more statistical correlations between the participating values must be considered. For the red/blue channel we must consider whether interpolation is performed on a green or a blue/red pixel. In the case of estimating the variance of a red value at a blue pixel, we used the previously estimated variance $(\sigma_{\text{add}}^{g\to b})^2$ of the interpolated green values. We also incorporated $(\sigma_{\text{add}}^{g\to r})^2$ in our calculations, since computation of K_R values at red neighboring pixels requires the usage of the interpolated green values at these positions. Because of the presence of $(\sigma_{\text{add}}^{g\to r})^2$ and $(\sigma_{\text{add}}^{g\to b})^2$ terms, the r_1 and r_2 coefficients were also incorporated. A coefficient r_1' is included to describe the correlation between the original green pixels and the K_R domain. Another coefficient, r_2', is included to describe the correlation between the interpolated green pixels and the K_R domain. To fully describe noise propagation for the red channel, we added one last coefficient to compensate for the correlation between the interpolated green and the red pixels, when estimating the $G-R$ domain. The derivation of variance for any chrominance channel x (c is the remaining chrominance channel), is similar to Eq. (55):

$$(\sigma_{\text{demos}}^x)^2 = \frac{1}{16}\{9(\sigma_o^x)^2 + 8(\sigma_o^g)^2 + 5(\sigma_{\text{add}}^{g\to x})^2 + 4(\sigma_{\text{add}}^{g\to c})^2 - (8\sqrt{2}r_1'\sigma_o^g + 4r_2'\sigma_{\text{add}}^{g\to c})[(\sigma_{\text{add}}^{g\to x})^2 - 2r_3\sigma_{\text{add}}^{g\to x}\sigma_o^x + (\sigma_o^x)^2]^{1/2} - 10r_3\sigma_{\text{add}}^{g\to y}\sigma_o^x\}, \tag{57}$$

where $(\sigma_{\text{add}}^{g\to r})^2$ and $(\sigma_{\text{add}}^{g\to b})^2$ are estimated using Eq. (54). If all participating values are uncorrelated ($r_1=r_2=r_1'=r_2'=r_3=0$) the preceding equation can be simplified:

$$(\sigma_{\text{demos}}^x)^2 = \frac{1}{128}[117(\sigma_o^x)^2 + 80(\sigma_o^g)^2 + 36(\sigma_o^c)^2]. \tag{58}$$

References

1. J. C. Trijonis, W. C. Malm, M. Pitchford, W. H. White, R. Charison, and R. Husar, "Visibility: existing and historical conditions—causes and effects," NAPAP Report 24, III, pp. 24/31 (Oct. 1990); available using http://vista.cira.colostate.edu/improve/Publications/publications.htm.
2. EPA, "Air quality criteria for particulate matter," II, EPA 600/P-95/001bF, pp. 8/1, 8/4, 8/79, 8/123–8/125 (Apr. 1996).
3. J. V. Molenar, W. C. Malm, and C. E. Johnson, "Visual air quality simulation techniques," *Atmos. Environ.* **28**(5), 1055–1063 (1994).
4. A. Eldering, S. M. Larson, J. R. Hall, K. J. Hussay, and G. R. Class, "Development of an improved image processing based visibility model," *Environ. Sci. Technol.* **27**(4), 626–635 (1993).
5. S. M. Larson and G. R. Cass, "Verification of image processing based visibility models," *Environ. Sci. Technol.* **22**(6), 629–637 (1988).
6. J. Hernándes-Andrés, R. L. Lee, Jr., and J. Romero, Jr., "Color and luminance asymmetries in the clear sky," *Appl. Opt.* **42**(3), 458–464 (2003).
7. J. L. Gardner, "Uncertainty estimation in colour measurement," *Color Res. Appl.* **25**, 349–355 (Oct. 2000).
8. P. L. Vora, J. E. Farrell, J. D. Tietz, and D. H. Brainard, "Image capture: simulation of sensor responses from hyperspectral images," *IEEE Trans. Image Process.* **10**(2), 307–315 (2001).
9. P. L. Vora, J. E. Farrell, J. D. Tietz, and D. H. Brainard, "Digital color cameras-1—response models," Technical Report HPL-97-53, Hewlett-Packard Co. (Mar. 1997).
10. P. L. Vora, J. E. Farrell, J. D. Tietz, and D. H. Brainard, "Digital color cameras-2—spectral response," Technical Report HPL-97-54, Hewlett-Packard Co. (Mar. 1997).
11. P. L. Vora, J. E. Farrell, J. D. Tietz, and D. H. Brainard, "Linear models for digital cameras," in *Proc. IS&T 50th Annu. Conf.*, pp. 377–382 (1997).
12. C. Kolb, D. Mitchell, and P. Hanrahan, "A realistic camera model for computer graphics," in *Proc. ACM SIGGRAPH*, pp. 317–324 (1995).
13. H. B. Wach and E. R. Dowski, Jr., "Noise modeling for design and simulation of color imaging systems, " in *Proc. IS&T 12th Color Imaging Conf.*, pp. 211–216 (2004).
14. T. Chen, "Digital camera system simulator and applications," PhD Thesis, Stanford University (2003).
15. J. E. Farrell, F. Xiao, P. B. Cartysse, and B. A. Wandell, "A simulation tool for evaluating digital camera image quality," *Proc. SPIE* **5294**, 124–131 (2004).
16. R. Lukac, K. N. Plataniotis, D. Hatzinakos, and M. Aleksic, "A novel cost effective demosaicing approach," *IEEE Trans. Consum. Electron.* **50**(1), 256–261 (2004).
17. R. Lukac and K. N. Plataniotis, "Normalized color-ratio modelling for CFA interpolation," *IEEE Trans. Consum. Electron.* **50**(2), 737–745 (2004).
18. B. Gunturk, Y. Altunbasak, and R. Mersereau, "Color plane interpolation using alternating projections," *IEEE Trans. Image Process.* **11**(9), 997–1013 (2002).
19. G. D. Finlayson and M. S. Drew, "Constrained least-squares regression in color spaces," *J. Electron. Imaging* **6**(4), 484–493 (1997).
20. B. E. Bayer, "Color imaging array," U.S. Patent No. 3,971,065 (Mar. 1976).
21. D. Litwiller, "CCD vs. CMOS: facts and fiction," *Photonics Spectra*, pp. 154–158 (Jan. 2001).
22. Eastman Kodak Co., "Conversion of light to electronic charge," CCD Primer, MTD/PS-0217 (May 2001); available using http://www.kodak.com/global/en/digital/ccd/.
23. R. E. Jacobson, S. F. Ray, and G. G. Attridge, *The Manual of Photography*, 8th ed., pp. 32, 50–52, Focal Press, London and Boston (1988).
24. Eastman Kodak Co., "KAF-5101CE image sensor. Device performance specification" (June 2003); available using http://www.kodak.com/global/en/digital/ccd/.
25. Eastman Kodak Co., "CCD image sensor noise sources," Application Note, MTD/PS-0233 (Aug. 2001) (online); available: http://www.kodak.com/global/en/digital/ccd/.
26. R. Ramanath, W. E. Snyder, G. L. Bilbro, and W. Sander, "Demosaicking methods for Bayer color arrays," *J. Electron. Imaging* **11**(3), 306–315 (2002).
27. T. Sakamoto, C. Nakanishi, and T. Hase, "Software pixel interpolation for digital still cameras suitable for a 32-bit MCU," *IEEE Trans.*

Consum. Electron. **44**(4), 1342–1352 (1998).
28. D. R. Cok, "Signal processing method and apparatus for producing interpolated chrominance values in a sampled color image signal," U.S. Patent No. 4,642,678 (1987).
29. S. C. Pei and I. K. Tam, "Effective color interpolation in CCD color filter arrays using signal correlation," *IEEE Trans. Circuits Syst. Video Technol.* **13**(6), 503–513 (2003).
30. R. Kimmel, "Demosaicing: image reconstruction from color CCD samples," *IEEE Trans. Image Process.* **8**(9), 1221–1228 (1999).
31. W. Lu and Y. P. Tang, "Color filter array demosaicing: new method and performance measures," *IEEE Trans. Image Process.* **12**(10), 1194–1210 (2003).
32. R. Lukac, B. Smolka, K. Martin, K. N. Plataniotis, and A. N. Venetsanopulos, "Vector filtering for color imaging," *IEEE Signal Process. Mag.* **22**(1), 74–86 (2005).
33. W. K. Pratt, *Digital Image Processing*, 2nd ed., p. 74, Wiley, New York (1991).
34. G. Sharma, *Digital Color Imaging*, pp. 30–38, 81, 291, 294, CRC Press, Boca Raton, FL (2003).
35. G. Sharma and H. J. Trussell, "Digital color imaging," *IEEE Trans. Image Process.* **6**(7), 901–932 (1997).
36. R. Philbrick, H. Erchardt, and H. Titus, "The efficiency of linear solid state imagers for film scanning applications," in *Proc. Mapping and Remote Sensing Tools for the 21st Century*, pp. 15–24, American Society for Photogrammetry and Remote Sensing (1994).
37. W. Wu and J. P. Allebach, "Imaging colorimetry using a digital camera," *J. Imaging Sci. Technol.* **44**(4), 267–279 (2000).
38. J. Teuber, *Digital Image Processing*, p. 26, Prentice Hall, UK (1993).
39. G. M. P. Centen, "CCD imaging: concepts for low noise and high bandwidth," Proefschrift, Technische Universiteit Eindhoven, pp. 7, 11, 21 (1999).
40. J. L. Gach, D. Darson, C. Guillaume, C. Goillandeau, O. Boissin, J. Boulesteix, and C. Cavadore, "Zero noise CCD: a new readout technique for extremely low light level observations," in *Scientific Drivers for ESO Future VLT/VLTI Instrumentation*, pp. 247–250, Springer, Berlin (2002).
41. G. C. Holst, *CCD Arrays, Cameras, and Displays*, 2nd ed., JCD Publishing and SPIE Optical Engineering Press, Bellingham, WA (1998).
42. J. K. Taylor, *Statistical Techniques for Data Analysis*, Lewis Publishers Inc. (1990).
43. R. Lukac, K. N. Martin, and K. N. Plataniotis, "Digital camera zooming based on unified CFA image processing steps," *IEEE Trans. Consum. Electron.* **50**(1), 15–24 (2004).
44. R. Lukac, K. Martin, and K. N. Plataniotis, "Demosaicked image postprocessing using local color ratios," *IEEE Trans. Circuits Syst. Video Technol.* **14**(6), 914–920 (2004).
45. S. K. Naik and C. A. Murthy, "Hue-preserving color image enhancement without gamut problem," *IEEE Trans. Image Process.* **12**(12), 1591–1598 (2003).
46. C. K. Dogras, M. P. Ioannidou, and D. P. Chrissoulidis, "Analytical study of the changes in the color of daylight due to sulfate droplets and soot grains in the atmosphere," *J. Quant. Spectrosc. Radiat. Transf.* **84**, 223–238 (Mar. 2004).
47. J. Sloup, "A survey of the modelling and rendering of the earth's atmosphere," in *Proc. of the 18th Spring Conf. on Computer Graphics*, A. Chalmers, Ed., pp. 141–150, ACM Press, NY (2002).
48. R. V. Klassen, "Modeling the effect of atmosphere on light," *ACM Trans. Graphics* **6**(3), 215–237 (1987).
49. X. F. Kneizys, P. E. Shettle, W. L. Abreu, H. J. Chetwynd, P. G. Anderson, O. W. Gallery, A. E. J. Selby, and A. S. Clough, *Users Guide to LOWTRAN 7*, USA Air Force Geophysics Lab., AFGL-TR-88-0177, Env. Res. Papers, no. 1010 (Aug. 1988).
50. J. Hernándes-Andrés and J. Romero, Jr., "Colorimetric and spectrometric characteristics of narrow-field-of-view clear skylight in Granada, Spain," *J. Opt. Soc. Am. A* **18**(2), 412–420 (2001).
51. P. D. Burns and R. S. Berns, "Error propagation analysis in color measurement and imaging," *Color Res. Appl.* **22**(4), 280–289 (1997).
52. B. A. Wandell and J. E. Farrel, "Water into wine: converting scanner RGB to tristimulus XYZ," *Proc. SPIE* **1909**, 92–100 (1993).

Panagiotis E. Haralabidis is a PhD candidate with the Department of Environment of the University of the Aegean. He received his BSc degree in physics and nonlinear dynamics of electric circuits from the University of Salonica, Greece. His research interests include atmospheric physics and aerosols, algorithms for digital color, and system simulation.

Christodoulos Pilinis received his diploma in chemical engineering from the National Technical University of Athens, Greece, in 1983, his MS degree in environmental engineering from Caltech, California, in 1984, and his PhD degree in environmental engineering and applied mathematics from Caltech, California, in 1988. He is an associate professor with the Department of Environment of the University of the Aegean, Mytilene, Greece.